

PREPARED FOR SUBMISSION TO JCAP

A systematic halo-independent analysis of direct detection data within the framework of Inelastic Dark Matter

Stefano Scopel,^a Kook-Hyun Yoon^b

Department of Physics, Sogang University, Seoul 121-742, South Korea

E-mail: scopel@sogang.ac.kr, koreasds@naver.com

Abstract. We present a systematic halo-independent analysis of available Weakly Interacting Massive Particles (WIMP) direct detection data within the framework of Inelastic Dark Matter (IDM). We show that, when the smallest number of assumptions is made on the WIMP velocity distribution in the halo of our Galaxy, it is possible to find values of the WIMP mass and the IDM mass splitting for which compatibility between present constraints and any of the three experiments claiming to see a WIMP excess among DAMA, CDMS-*Si* and CRESST can be achieved.

Contents

1	Introduction	1
2	Factorization of the halo model dependence	3
3	Phenomenological analysis: the case of elastic scattering	6
4	Halo-independent tests for Inelastic Dark Matter	8
4.1	Internal consistency checks	10
4.2	Comparison among different experiments	13
5	Phenomenological analysis: the case of inelastic scattering	13
5.1	Sodium scattering in DAMA and the CDMS- <i>Si</i> excess	14
5.2	Iodine scattering in DAMA and the CRESST excess	18
5.3	Sodium scattering in DAMA at large WIMP masses	25
6	Conclusions	27
A	Experimental inputs for the analysis	29

1 Introduction

Weakly Interacting Massive Particles (WIMPs) are among the best motivated and most popular candidates to provide the Dark Matter that is believed to constitute about 27% of the total mass density of the Universe, as confirmed by the latest measurement of cosmological parameters[1]. Presently, WIMPs are searched for by a plethora of direct detection experiments, which look for the tiny recoil energy E_R imparted to the nuclei of a low-background underground detector by the particles that are expected to constitute the dark halo of our Galaxy. Due to the small expected E_R (in the keV range) and the tiny expected cross sections with ordinary nuclei (10^{-42} cm² or less in most popular scenarios) detecting WIMPs is experimentally challenging. The present experimental situation is quite elaborate, with two experiments claiming evidence for a yearly modulation in their data attributable to a WIMP signal (DAMA[2], CoGeNT[3]), other two claiming a non-observation in their modulation data (CDMS[4] and KIMS[5]), some others claiming a possibly WIMP-induced excess in their time-averaged event spectra in tension with background estimates (CoGeNT[6], CDMS-*Si* [8], CRESST [9]) and many other experimental collaborations not observing any discrepancy with the estimated background and as a consequence publishing constraints that, when interpreted in specific WIMP scenarios, are in (sometimes strong) tension with the aforementioned results (LUX[10], XENON100[11], XENON10[12], KIMS[13], CDMS-*Ge*[14], CDMSlite [15], SuperCDMS[16]).

Until recently, the standard approach to interpret the results of direct detection experiments in terms of a WIMP signal was to assume for the WIMPs a specific velocity distribution in the Galactic reference frame: in particular the usual assumption is the Isothermal Sphere Model, i.e. a Maxwellian representing a WIMP gas in thermal equilibrium with r.m.s. velocity $v_{rms} \simeq 270$ km/sec and a velocity upper cut representing the escape velocity. As suggested in Ref.[17], however, when recoil energy intervals analyzed by different

experiments are mapped into same ranges for the minimal velocity v_{min} that the incoming WIMP needs to have to deposit E_R the halo model dependence can be factorized. Following [17] several analyzes have been performed to compare the results of different experiments in terms of WIMP elastic scattering without making specific assumptions on the WIMP velocity distribution[18, 19].

A scenario proposed to alleviate the tension among different direct detection experiments is Inelastic Dark Matter (IDM)[20]. In this class of models a Dark Matter (DM) particle χ of mass m_{DM} interacts with atomic nuclei exclusively by up-scattering to a second state χ' with mass $m'_{DM} = m_{DM} + \delta$. In the case of exothermic Dark Matter [21] $\delta < 0$ is also possible: in this case the particle χ is metastable and down-scatters to a lighter state χ' .

In both cases making use of the halo-model factorization approach is significantly more complicated compared to the elastic case, because when $\delta \neq 0$ the mapping from E_R to v_{min} becomes more involved than in the elastic case, introducing several complications: for instance there is no longer a one-to-one correspondence between E_R and v_{min} . So, while some early attempts exist [22], a systematic analysis of IDM where an assessment of all the available data is done making use of the factorization property of the halo-model dependence is still missing. In the present paper we wish to address this issue, introducing some strategies to determine regions in the IDM parameter space where the tension existing among different experimental results can be (at least partially) alleviated, and analyzing in detail some specific benchmarks. In particular, by assuming a standard Maxwellian WIMP velocity distribution, present data from XENON100[23] appear to already exclude an interpretation of the DAMA modulation effect in terms of the IDM hypothesis: as we will see, in specific cases the halo-dependence factorization approach can indeed allow instead to find regions of the IDM parameter space which are mutually compatible between DAMA and liquid Xenon detectors. However this approach can only be effective when experimental results obtained using different detector targets are compared. In fact, it is obvious that conflicting results obtained with same-target detectors cannot be brought into agreement by any theoretical assumption on the WIMP-nucleus scattering process, including IDM. This is for instance the case for the apparent tension between the DAMA[2] modulation result interpreted in terms of WIMP-Iodine scatterings and the KIMS[13] claim of non-observation of a WIMP excess with a CsI target. Something similar happens between the CoGeNT excesses[3, 6] and upper bounds obtained by other germanium detectors. In this case the only way to reconcile conflicting results is to look deeper in the possible sources of systematic errors, including the many uncertainties connected to quenching factors, atomic form factors, background cuts efficiencies, etc.[24].

In the following we chose to extend our analysis of IDM to $\delta < 0$. Notice however, that while this scenario can indeed explain the excesses observed in the unmodulated spectra of direct detection experiments (for instance it has been recently proposed to explain the three WIMP-candidate events observed by CDMS-Si [25]) in this regime DM is expected to produce a very suppressed yearly modulation signal[21]: in fact, when the kinetic energy of the incoming WIMP is below the mass splitting $|\delta|$ the deposited recoil energy E_R is determined solely by the energy deposited in the exothermic process, and is independent on the WIMP incoming velocity. In this case if a yearly modulation is observed, it can hardly be produced by the boost from the galactic to the Earth rest frame. As far as this aspect is concerned, we adopt a purely phenomenological approach and chose to extend our analysis of the DAMA modulation excess to $\delta < 0$ without any theoretical prejudice¹.

¹In principle, a yearly modulation could still arise from some solar-system scale features in the DM spatial

The paper is organized as follows: in Section 2 we summarize the halo-model factorization technique in WIMP–nucleus scattering (also pointing out some of its limitations) and discuss the problematics emerging in the context of IDM; in Section 3 we show the present situation in the case of elastic scattering; in Section 4 we introduce some tests to analyze the data which are specific to IDM; Section 5 contains the quantitative results of this paper with a phenomenological discussion of the present experimental results in the context of IDM; finally, in Appendix A we summarize the experimental inputs used in the analysis.

2 Factorization of the halo model dependence

In the IDM scenario, in order to deposit the recoil energy E_R in the detector the incoming WIMP velocity v (in the laboratory rest frame) needs to be larger than the minimal speed v_{min} :

$$v_{min} = \frac{1}{\sqrt{2m_N E_R}} \left| \frac{m_N E_R}{\mu_{\chi N}} + \delta \right|, \quad (2.1)$$

where m_N is the mass of the nucleus and $\mu_{\chi N}$ is the WIMP–nucleus reduced mass. Given a detector using a mono-atomic target with active mass M and exposition time T the expected differential rate for WIMP scatterings depositing the recoil energy E_R is given by:

$$\frac{dR}{dE_R} = MT \frac{\rho_{DM}}{m_{DM}} \sigma_0 \frac{N_T m_N \tilde{A}^2}{2\mu_{\chi N}^2} F^2(E_R) \eta(v_{min}), \quad (2.2)$$

where ρ_{DM} is the DM mass density in the neighborhood of the Sun, N_T is the number of targets per unit mass, $\mu_{\chi N}$ is the WIMP–nucleon (proton or neutron) reduced mass, while:

$$\sigma_0 \equiv \lim_{v \rightarrow \infty} \sigma_p = \frac{\sigma_p}{\sqrt{1 - \frac{2|\delta|}{\mu_{\chi N} v}}}, \quad (2.3)$$

with σ_p the WIMP–proton point-like cross section². Moreover \tilde{A} is the ratio between the WIMP–nucleus and the WIMP–proton interaction amplitudes. In particular, in the present paper we will assume the scaling law for a scalar-coupling interaction:

$$\tilde{A} = Z + (A - Z) \frac{f_n}{f_p}, \quad (2.4)$$

where f_n/f_p represents the ratio between the coupling of the χ particle to neutrons and protons, respectively, while Z and A are the atomic number and mass number of the target nucleus. In Eq.(2.2) $F(E_R)$ is a form factor taking into account the finite size of the nucleus for which we assume the standard form[26]:

$$F(E_R) = \frac{3}{qR'} \left[\frac{\sin(qR')}{(qR')^2} - \frac{\cos(qR')}{qR'} \right] \exp\left(-\frac{(qs)^2}{2}\right) \quad (2.5)$$

$$q = \sqrt{2m_N E_R}; \quad R' = \sqrt{R_N^2 - 5s^2}; \quad R_N = 1.2A^{\frac{1}{3}}; \quad s = 1 \text{ fm}. \quad (2.6)$$

distribution.

²In the IDM case σ_p maintains a dependence on v also in the non-relativistic limit, $\sigma_p \propto \sqrt{1 - 2|\delta|/(\mu_{\chi N} v)}$, but the dependence cancels out when calculating the differential cross section $d\sigma_p/dE_R$. For this reason the cross section factorized in Eq.(2.2) is σ_0 and not directly σ_p .

Finally, in equation (2.2) the function:

$$\eta(v_{min}) = \int_{|\vec{v}| > v_{min}} \frac{f(\vec{v})}{|\vec{v}|} d^3v, \quad (2.7)$$

contains the dependence of the expected rate on the velocity distribution $f(\vec{v})$ (boosted in the laboratory reference frame).

Eq. (2.2) can then be recast in the form:

$$\frac{dR}{dE_R}[E_R(v_{min})] = MT \frac{N_T m_N \tilde{A}^2}{2\mu_{\chi\mathcal{N}}^2} F^2(E_R) \tilde{\eta}(v_{min}), \quad (2.8)$$

where the quantity:

$$\tilde{\eta}(v_{min}) \equiv \frac{\rho_{DM}}{m_{DM}} \sigma_0 \eta(v_{min}), \quad (2.9)$$

is a factor common to the WIMP–rate predictions of all experiments, provided that it is sampled in the same intervals of v_{min} . Mutual compatibility among different detectors' data can then be investigated (factorizing out the dependence on the halo velocity distribution) by binning all available data in the same set of v_{min} intervals and by comparing the ensuing estimations of $\tilde{\eta}(v_{min})$.

In Eq.(2.7) $f(\vec{v})$ represents the WIMP velocity distribution boosted from the Galactic rest frame to the reference frame of the laboratory. The involved boost depends on the velocity of the Earth in the Galactic rest frame. Since the latter is the result of the combination of the motion of the Solar system and of the rotation of the Earth around the Sun a yearly time modulation is predicted that can be used to discriminate between signal and background in direct dark matter searches. In particular, in the case of a Maxwellian WIMP velocity distribution this time dependence can be approximated with the functional form:

$$\tilde{\eta}_{Maxwellian}(t) \simeq \tilde{\eta}_{Maxwellian,0} + \tilde{\eta}_{Maxwellian,1} \cos[\omega(t - t_0)], \quad (2.10)$$

where $\omega = 2\pi/365$ days, the phase $t_0 \simeq 2$ of June corresponds to the moment when the velocity of the Sun in the Galactic rest frame and the velocity of the Earth around the Sun point in the same direction (leading to a maximum in the relative flux of incoming WIMPS impinging on the detector) and the ratio $\tilde{\eta}_{Maxwellian,1}/\tilde{\eta}_{Maxwellian,0}$ is predicted to be between 5% and 10%. Experiments sensitive to this yearly modulation (such as DAMA and CoGeNT) actually provide estimations of the modulated halo functions $\tilde{\eta}_1$ using the above time–dependence, while the others get either estimations or upper bounds on the unmodulated halo functions $\tilde{\eta}_0$. Notice however that, while the sinusoidal time dependence of the expected rate given in Eq.(2.10) is used by DAMA and CoGeNT to analyze their modulation data, this is not the only possible one, not even, for instance, in anisotropic extensions of the isothermal sphere [27]. Actually, strictly speaking the only halo model independent definitions of the unmodulated and modulated parts of the $\tilde{\eta}$ functions are simply:

$$\begin{aligned} \tilde{\eta}_0 &\equiv \langle \tilde{\eta}(\Delta T = 1 \text{ year}) \rangle \\ \tilde{\eta}_1 &\equiv \frac{\langle \tilde{\eta}(\Delta T_1) \rangle - \langle \tilde{\eta}(\Delta T_2) \rangle}{2}, \end{aligned} \quad (2.11)$$

where $\langle \rangle$ represents time average, and ΔT_1 , ΔT_2 are two equal time intervals centered around the maximum and minimum of the signal, whose phase should be determined directly from the data and common to the analysis of the experiments that are compared³.

As a consequence of the above discussion, estimations of the $\tilde{\eta}_1$ halo function which make use of annual modulation amplitudes published by experimental collaborations are not really halo independent, since their validity is restricted to the class of halo models with the specific time dependence of Eq.(2.10). Nevertheless, in the following we will make use of the published DAMA modulation amplitudes to estimate the $\tilde{\eta}_1$ function, implicitly assuming that indeed the $\tilde{\eta}_{Maxwellian,1}$ estimations obtained using the time dependence (2.10) do not differ significantly from what one would obtain using Eq.(2.11) to analyze the data.

In a real-life experiment E_R is obtained by measuring a related detected energy E' obtained by calibrating the detector with mono-energetic photons with known energy. However the detector response to photons can be significantly different compared to the same quantity for nuclear recoils. For a given calibrating photon energy the mean measured value of E' is usually referred to as the electron-equivalent energy E_{ee} and measured in keVee. On the other hand E_R (that represents the signal that would be measured if the same amount of energy were deposited by a nuclear recoil instead of a photon) is measured in keVnr. The two quantities are related by a quenching factor Q according to $E_{ee} = Q(E_R)E_R$ ⁴. Moreover the measured E' is smeared out compared to E_{ee} by the energy resolution (a Gaussian smearing $Gauss(E_{ee}|E', \sigma_{rms}(E')) \equiv 1/(\sigma_{rms}\sqrt{2\pi})\exp[-(E' - E_{ee})^2/(2\sigma_{rms}^2)]$ with standard deviation $\sigma_{rms}(E')$ related to the Full Width Half Maximum (FWHM) of the calibration peaks at E' by $FWHM = 2.35\sigma_{rms}$ is usually assumed) and experimental count rates depend also on the counting efficiency or cut acceptance $\epsilon(E')$. Overall, the expected differential event rate is given by:

$$\frac{dR}{dE'} = \epsilon(E') \int_0^\infty dE_{ee} Gauss(E_{ee}|E', \sigma_{rms}(E')) \frac{1}{Q(E_R)} \frac{dR}{dE_R}. \quad (2.12)$$

In the case of liquid scintillators it is customary to measure both the observed signal and its mean value directly in PE (photoelectrons) and to parametrize the quenching factor in terms of an effective light yield $\mathcal{L}_{eff}(E_R)$ normalized at the calibrating energy of 122 keV. Moreover, lacking a direct calibration at low energy the resolution is estimated assuming a Poisson fluctuation for the photoelectrons and folding it with the Gaussian response of the photomultiplier[28] (see Appendix A for details).

Combining Eqs.(2.2) and (2.12) the expected number of events in the interval $E'_1 < E' < E'_2$ can be cast in the form:

$$N_{theory}(E'_1, E'_2) = \int_{E'_1}^{E'_2} dE' \frac{dR}{dE'} = \int_0^\infty dE_{ee} \tilde{\eta} \{v_{min}[E_R(E_{ee})]\} \mathcal{R}_{[E'_1, E'_2]}(E_{ee}), \quad (2.13)$$

where the response function \mathcal{R} , given by:

³Time averages of different experiments should be obtained using overlapping periods of data taking.

⁴The quenching factor is measured with a neutron source, and is subject to large uncertainties especially at low energies. Moreover, to avoid nuclear activation it is not measured in the same low-background detectors used for WIMP-search data. This is potentially a major source of systematics since Q may depend on the operating experimental conditions and can vary in different detectors of the same material.

$$\mathcal{R}_{[E'_1, E'_2]}(E_{ee}) = \frac{N_T m_N \tilde{A}^2}{2\mu_{\chi N}^2} F^2 [E_R(E_{ee})] MT \int_{E'_1}^{E'_2} dE' \text{Gauss}(E_{ee}|E', \sigma_{rms}(E')) \epsilon(E'), \quad (2.14)$$

contains the information of each experimental setup. Given an experiment with detected count rate N_{exp} in the energy interval $E'_1 < E' < E'_2$ the combination:

$$\bar{\eta} = \frac{\int_0^\infty dE_{ee} \tilde{\eta}(E_{ee}) \mathcal{R}_{[E'_1, E'_2]}(E_{ee})}{\int_0^\infty dE_{ee} \mathcal{R}_{[E'_1, E'_2]}(E_{ee})} = \frac{N_{exp}}{\int_0^\infty dE_{ee} \mathcal{R}_{[E'_1, E'_2]}(E_{ee})}, \quad (2.15)$$

can be cast in the form[19]:

$$\bar{\eta} = \frac{\int_0^\infty dv_{min} \tilde{\eta}(v_{min}) \mathcal{R}_{[E'_1, E'_2]}(v_{min})}{\int_0^\infty dv_{min} \mathcal{R}_{[E'_1, E'_2]}(v_{min})} = \frac{N_{exp}}{\int_0^\infty dv_{min} \mathcal{R}_{[E'_1, E'_2]}(v_{min})}, \quad (2.16)$$

by changing variable from E_{ee} to v_{min} (in the above expression $\mathcal{R}_{[E'_1, E'_2]}(v_{min}) = \mathcal{R}_{[E'_1, E'_2]}(E_{ee}) dE_{ee}/dv_{min}$) and can be interpreted as an average of the function $\tilde{\eta}(v_{min})$ in an interval $v_{min,1} < v_{min} < v_{min,2}$. The latter is defined as the one where the response function \mathcal{R} is “sizeably” different from zero (we will conventionally take the interval $v_{min}[E_R(E_{ee,1})] < v_{min} < v_{min}[E_R(E_{ee,2})]$ with $E_{ee,1} = E'_1 - \sigma_{rms}(E'_1)$, $E_{ee,2} = E'_2 + \sigma_{rms}(E'_2)$, i.e. the E' interval enlarged by the energy resolution).

The formalism summarized in this Section is no longer straightforward in the case of experiments that use multi-atomic targets, unless it is possible to conclude that only one of them dominates the scattering⁵. This is the case of NaI in DAMA, where for the elastic case it is possible to conclude that the v_{min} range required to explain scatterings off the Iodine nuclei is above reasonable values of the escape velocity for $m_{DM} \lesssim 20$ GeV, so that at low WIMP masses domination of scatterings off Na nuclei can be established; on the other hand at larger masses, assuming the scaling law in (2.4) with $f_n/f_p = 1$, scatterings on Iodine are automatically guaranteed to be predominant (see Fig.12 and discussion in Section 3). However, in the case of inelastic scattering the situation is more involved, as will be discussed at the end of Section 5.

The factorization procedure described above can be separately applied in a straightforward way to get estimates $\bar{\eta}_0$ and $\bar{\eta}_1$ of the constant and modulated parts of the $\bar{\eta}$ function. As already pointed out before, however, we wish to remark again that in the case of the modulated part experimental amplitudes are usually extracted by assuming the time dependence of Eq.(2.10), limiting *de facto* the scope of a “halo-independent” analysis to a restricted (albeit well motivated) class of models.

3 Phenomenological analysis: the case of elastic scattering

In Figures 1 and 2 we summarize the present experimental situation for the determination of the $\bar{\eta}_0$ and $\bar{\eta}_1$ functions in the case of elastic scattering ($\delta = 0$) as a function of v_{min} for the two representative values $m_{DM}=8$ GeV and $m_{DM}=100$ GeV. In both figures we adopt $f_n/f_p=1$, assuming in DAMA scatterings on Na when $m_{DM}=8$ GeV and scattering on I when $m_{DM}=100$ GeV.

⁵The case of two targets very close in mass is one exception: see Appendix A for a discussion of *CsI* in KIMS[13].

We include in the analysis the following experiments: DAMA[2], CoGeNT [6], CDMS-Si[8], XENON100[11], LUX [10] SuperCDMS [16] XENON10 [12], CDMSlite [15], CDMS-Ge [14], CRESST[9], KIMS[13]. The details of the parameters used to evaluate the response function of each experiment are summarized in Appendix A.

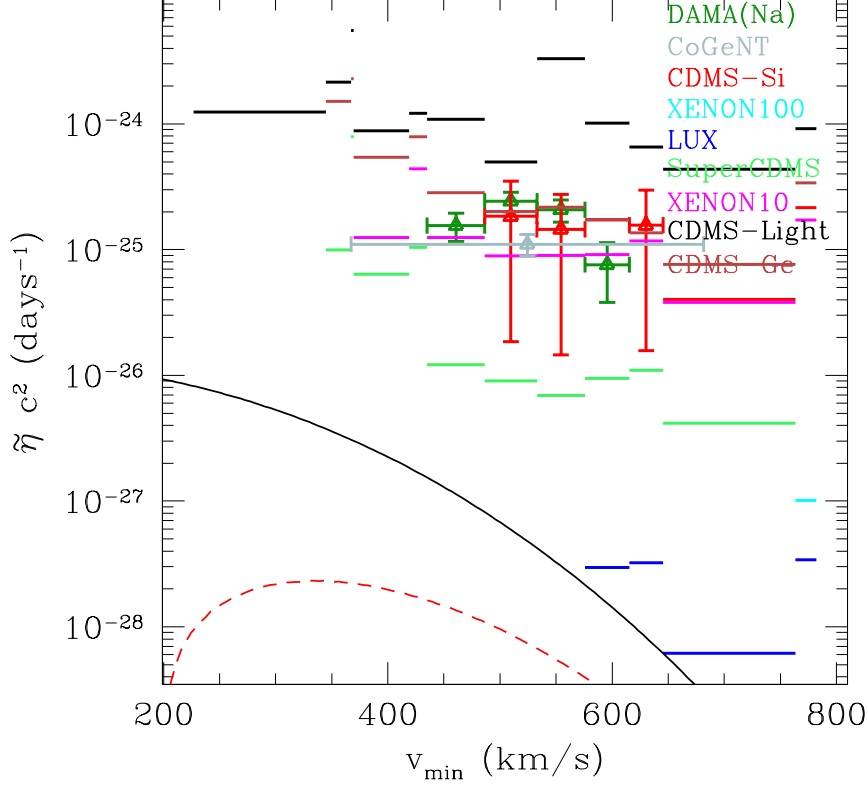


Figure 1. Measurements and bounds for the functions $\tilde{\eta}_0, \tilde{\eta}_1$ defined in Eq.(2.11) for $m_{DM}=8$ GeV, $\delta=0$ (elastic scattering) and $f_p = f_n=1$. Open triangles represent excesses that can be interpreted as WIMP signal candidates (the vertical error bars are at 1σ) while horizontal lines represent 90% C.L. upper bounds from experiments that did not observe any excess. The solid (black) and dashed (red) lines represent the predictions for $\tilde{\eta}_0$ and $\tilde{\eta}_1$, respectively, for a Maxwellian velocity distribution, normalized to the most constraining upper bound.

In this Section and in the following ones we choose to map all the experimental data in the same v_{min} intervals, in order to directly compare different determinations of the same quantities $\tilde{\eta}_{0,1}$ averaged within identical ranges of v_{min} . Since DAMA is the experiment with the highest accumulated statistics and the strongest indication of a possible WIMP signal we rebin the data of all other experiments in the v_{min} intervals corresponding to the energy bins of DAMA. Outside the v_{min} range covered by DAMA we bin the data using the collection of v_{min} values obtained considering for each experiment the energy boundary of the corresponding Region Of Interest (ROE) $= [E_{min}, E_{max}]$ and collecting the two v_{min} values corresponding to E_{min} and E_{max} . This automatic binning procedure implies that in Figs. 1 and 2 of this Section and in the analogous figures in the following ones some velocity bins may happen to be small, so that, depending on the resolution of the plots, some of the $\tilde{\eta}_{0,1}$ determinations or upper bounds may appear as dots.

In agreement with previous analyzes[19], taken at face value the results of Figs. 1 and 2

show a strong tension among different results. In particular, the null results of SuperCDMS, LUX and XENON100 imply constraints on $\tilde{\eta}_0$ which are about one and two orders of magnitude smaller compared to the $\tilde{\eta}_1$ ranges suggested by DAMA, or the $\tilde{\eta}_0$ ranges suggested by CDMS-*Si*, CRESST or CoGeNT⁶. Moreover, for $m_{DM} = 8$ GeV there also appears to be tension among the DAMA and CDMS-*Si* excesses, with the $\tilde{\eta}_1$ ranges indicated by DAMA in the upper range of the $\tilde{\eta}_0$ values suggested by CDMS-*Si*. Finally, in Fig. 2, where the DAMA excess is explained by WIMP-*I* scatterings, the KIMS upper bound is in tension with the DAMA modulation data. As already anticipated in the Introduction, this discrepancy cannot be alleviated by assuming a different scenario for the WIMP-nucleus interaction and will persist in the IDM case discussed in Section 5 whenever WIMP-*I* scatterings are assumed in DAMA. The same happens for the apparent discrepancy between the CoGeNT excess and the SuperCDMS bound, which both use Germanium targets.

The tension discussed above is even stronger if a Maxwellian is assumed for the velocity distribution: in both Figs. 1 and 2 the solid and dashed lines represent the corresponding predictions for $\tilde{\eta}_0$ and $\tilde{\eta}_1$, respectively, normalized to the most constraining limit. In this case, for instance, the DAMA result stands between two and three orders of magnitude above the maximal value of $\tilde{\eta}_1$ compatible to the LUX upper bound. In the following Sections we will discuss possible strategies to relieve (at least partially) the observed discrepancies discussed above within the context of IDM and if the smallest possible number of theoretical assumptions is made on the functions $\tilde{\eta}_0$ and $\tilde{\eta}_1$.

4 Halo-independent tests for Inelastic Dark Matter

A complication of the IDM case compared to elastic scattering is that the mapping between v_{min} and E_R (and so E') from Eq. (2.1) is no longer univocal. In particular v_{min} has a minimum when $E_R = E_R^* = |\delta| \mu_{\chi N} / m_N$ given by:

$$v_{min}^* = \begin{cases} \sqrt{\frac{2|\delta|}{\mu_{\chi N}}} & \text{if } \delta > 0 \\ 0 & \text{if } \delta < 0, \end{cases} \quad (4.1)$$

and any interval of $v_{min} > v_{min}^*$ corresponds to two mirror intervals for E_R with $E_R < E_R^*$ or $E_R > E_R^*$. As a consequence of this when $E_{ee}(E_R^*) \in [E_{ee,1}, E_{ee,2}]$ the change of variable from Eq.(2.15) to Eq.(2.16) leads to two disconnected integration ranges for v_{min} and to an expression of N_{theory} in terms of a linear combination of the corresponding two determinations of $\tilde{\eta}$. This problem can be easily solved by binning the energy intervals in such a way that for each experiment the energy corresponding to $E_{ee}(E_R^*)$ is one of the bin boundaries. So we generalize the v_{min} binning procedure described in Section 3: first we rebin (if needed) the DAMA data, starting from $E_{ee}(E_R^*)$ and selecting “mirror” energy intervals lower and higher than $E_{ee}(E_R^*)$ in such a way that they correspond to equal v_{min} ranges (we adopt the requirement that the smallest of the two mirror bins so obtained is equal to 0.5 keV and discard smaller values). Outside the v_{min} range covered by DAMA we bin the data using the collection of v_{min} values obtained considering for each experiment the energy boundary of the corresponding Region Of Interest= $[E_{min}, E_{max}]$ and collecting the three (two) v_{min}

⁶It should be noted that the LUX and XENON100 bounds for $m_{DM}=8$ GeV are obtained by using the low-energy part of the spectrum ($S_1 < 3$ PE), where the sensitivity of liquid scintillators has been put into question [24]. However also the SuperCDMS and XENON10 data appear constraining, albeit to a somewhat less extent. In particular, the energy range determining the SuperCDMS bound is $E_R < 7$ keV while the corresponding one for XENON10 is $E_R < 4.3$ keV. See Appendix A for details on various experiments.

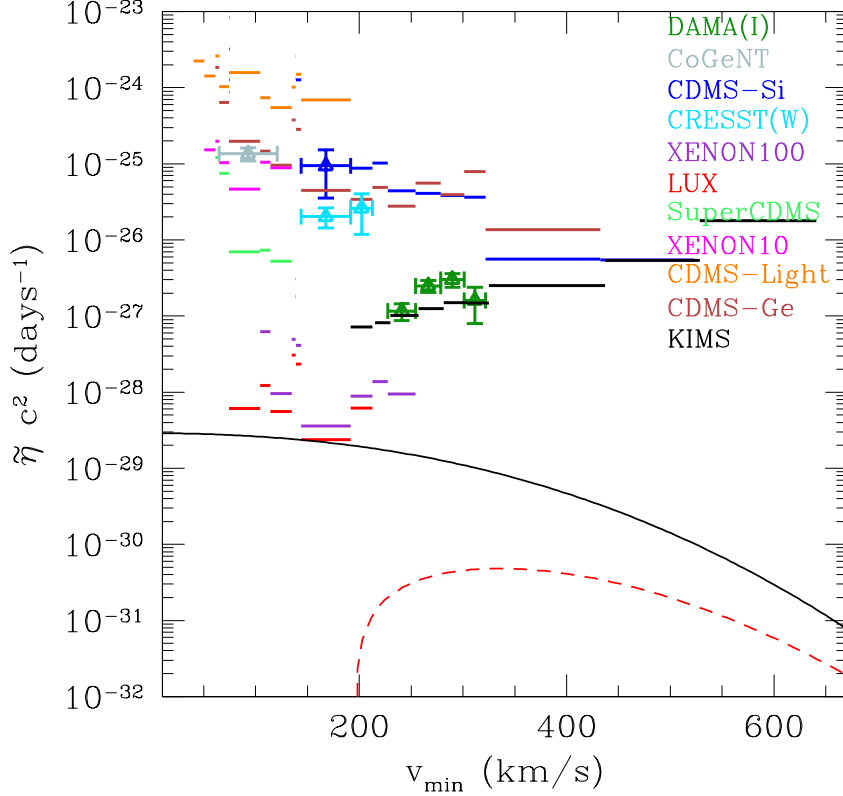


Figure 2. The same as in Fig.1 with $m_{DM}=100\text{GeV}$.

values corresponding to v_{min}^* (when applicable) and to E_{min} , E_{max} . In the case $\delta \neq 0$ this procedure ensures that $E_{ee}(E_R^*) \notin [E_{ee,1}, E_{ee,2}]$ for all the shown data. Provided that $E_{ee}(E_R^*) \notin [E_{ee,1}, E_{ee,2}]$ the procedure to determine the $\tilde{\eta}$ averages is then similar to the elastic case.

In particular the change of variable from E_{ee} to v_{min} leading to Eq. (2.16) depends now on the δ parameter, so that the response function \mathcal{R} not only depends on the target mass m_N but also on δ . However, it is clear that given an energy interval and a corresponding experimental count rate the denominator of Eq.(2.15) does not depend on δ . The only effect of a change of δ is then a shift in the corresponding v_{min} range.

We notice here that, with the exception of DAMA and KIMS, all the experiments that we will discuss in the following have made their count rates public so that rebinning their data according to the required v_{min} ranges will be straightforward. In the case of the DAMA data, whenever possible we will make direct use of the binned modulated amplitudes published by the Collaboration[2] and map all the other experimental results in those bins. Notice however that, as explained above, we will need to rebin also the DAMA data whenever, on Sodium or Iodine, $E_{ee}(E_R^*) \in [E_{ee,1}, E_{ee,2}]$. This would require to have the raw count rates. However, given the large statistics of the DAMA data we decide to proceed by averaging the binned modulated amplitudes $S_{m,k}$ taken from [2] in the new energy bins using the expression:

$$S_m^{rebinned}(E_{min}, E_{max}) = \frac{1}{\Delta E} \sum_k \bar{\Delta} E_k S_{m,k}, \quad (4.2)$$

where $\Delta E = E_{min} - E_{max}$ is the width of the new bin and $\bar{\Delta E}_i$ is the overlap between ΔE and the original bin $\Delta E_i = E_{i+1} - E_i$. To get an estimate of the fluctuation on $S_m^{rebinned}$ we conservatively use the above formula where the $S_{m,i}$ are replaced by their corresponding 1- σ upper and lower values as taken from [2]. We will adopt the same procedure also when rebinning the KIMS data.

For later convenience, let us now introduce some notation that will be useful in the following Sections. We will follow the convention of naming v_{min} intervals using capital-lettered names starting with V (for instance, $V_DAMA_NA \equiv [v_1^{DAMA,Na}, v_2^{DAMA,Na}]$) and the corresponding energy intervals with the same name where the initial V is substituted by an E, using an arrow to indicate the mapping of one into the other. Moreover, since for $\delta \neq 0$ each energy interval has a mirror one corresponding to the same v_{min} range we will add an initial M_ to the name of an energy interval to indicate it. So: $V_DAMA_NA \rightarrow E_DAMA_NA, M_E_DAMA_NA$ ⁷. Moreover we will combine intervals using logical and simple mathematical symbols (for instance, $V1 \cap V2 > V3$ means that the v_{min} values belonging to the overlapping of V1 and V2 are all larger than those belonging to V3).

In the present analysis we wish to make the smallest possible number of assumptions on the two functions $\tilde{\eta}_0$ and $\tilde{\eta}_1$. In particular, they reduce to:

$$\begin{aligned} \tilde{\eta}_0(v_{min,2}) &\leq \tilde{\eta}_0(v_{min,1}) \text{ if } v_{min,2} > v_{min,1}, \\ \tilde{\eta}_1 &\leq \tilde{\eta}_0 \quad \text{at the same } v_{min}, \\ \tilde{\eta}_0(v_{min} \geq v_{esc}) &= 0. \end{aligned} \tag{4.3}$$

The first condition descends from the definition (2.7), that implies that $\tilde{\eta}(v_{min})$ is a decreasing function of v_{min} . The second is an obvious consequence of the fact that $\tilde{\eta}_1$ is the modulated part of $\tilde{\eta}$. The last condition reflects the requirement that the WIMPs are gravitationally bound to our Galaxy. In the following we will assume that the WIMP halo is at rest in the Galactic rest frame and we will adopt as the maximal velocity of WIMPs $v_{esc} = 782$ km/s in the reference frame of the laboratory, by combining the reference value of the escape velocity $v_{esc}^{Galaxy} = 550$ km/s in the galactic rest frame with the velocity $v_0 = 232$ km/s of the Solar system with respect to the WIMP halo. Note that the specific value of the escape velocity is relevant at low values of m_{DM} , for which positive excesses can be explained by ranges of v_{min} close to v_{esc} . For each of the benchmarks discussed in the following the relevance of v_{esc} will be easily read-off from the corresponding $v_{min} - \tilde{\eta}_{0,1}$ plot.

4.1 Internal consistency checks

We describe here two internal checks (i.e. involving the data of one single experiment) that we will apply in a systematic way in the discussion of Section 5.

Suppose that a direct detection experiment observes an excess potentially attributable to a WIMP signal in the energy range E_SIG (this will require the additional condition $E_SIG \rightarrow V_SIG \in V_GAL \equiv [0, v_{esc}]$). Then, according to the discussion below Eq. (4.1), if $E^* \in E_SIG$ (where E^* is defined above Eq.(4.1)) the interval E_SIG must be split into two sub-intervals E_SIG1 and E_SIG2 , with $E_SIG1 \rightarrow [v_{min}^*, v_{min}^1] \equiv V_STAR1$ and $E_SIG2 \rightarrow [v_{min}^*, v_{min}^2] \equiv V_STAR2$. Then, if for instance $V_STAR1 \subset V_STAR2$ one has $M_E_SIG1 \subset E_SIG2$, and $E_SIG1, M_E_SIG1 \rightarrow V_STAR1$, i.e. the two intervals allow for independent determinations

⁷If the mirror interval of the signal range does not belong to the ROE a one-to-one correspondence between v_{min} and the recoil energy is recovered.

of the function $\tilde{\eta}_0$ or $\tilde{\eta}_1$ in the same v_{min} interval (by the same token if instead $V_STAR2 \subset V_STAR1$ then $E_SIG2, M_E_SIG2 \rightarrow V_STAR2$). This procedure allows to perform a compatibility check, as already pointed out in [22]. In the following we will refer to this procedure as the “shape test”.

Notice that the shape test can be effective only in the (small) range of the m_{DM} and δ parameters where $E^* \in E_SIG$. Actually, a more general and potentially more constraining test can be devised when $E^* \notin E_SIG$ and the mirror interval M_E_SIG of E_SIG corresponds to an energy range where no signal has been detected. Let us indicate with E_ROE the complete energy interval analyzed by the experiment. Then, the two mirror intervals $E_SIG_ROE \equiv M_E_SIG \cap E_ROE$ and $M_E_SIG_ROE \in E_SIG$ correspond to the same v_{min} interval and allow to perform a compatibility test analogous to the shape test. In the following we apply this procedure referring to it as the “mirror test”. For the sake of clarity, we schematically outline this procedure in Fig. 3 for $m_{DM}=100$ GeV, $\delta=75$ keV in the specific case of Tungsten in CRESST, where (see Appendix A) $E_ROE=[10 \text{ keV}, 40 \text{ keV}]$ and $E_SIG=[12 \text{ keV}, 24 \text{ keV}]$.

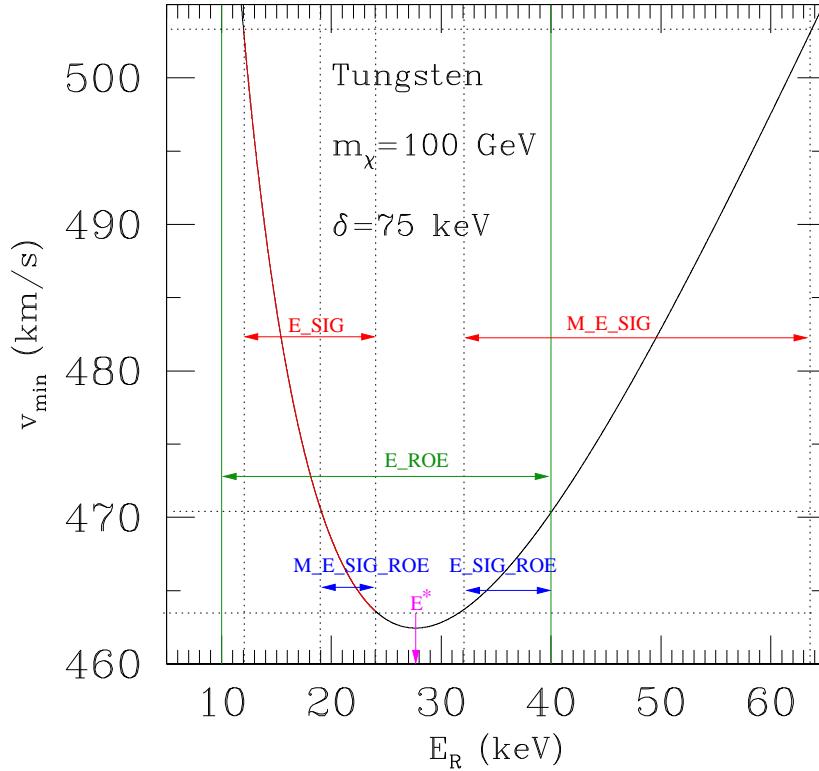


Figure 3. Schematic view of the mirror test introduced in Section 4, for $m_{DM}=100$ GeV, $\delta=75$ keV in the specific case of Tungsten in CRESST. The red part of the parabolic curve corresponds to the energy range [12 keV, 24 keV] of the CRESST excess, while the interval $E_R=[10 \text{ keV}, 40 \text{ keV}]$ corresponds to the analyzed Region of Interest (see Appendix A).

We notice here that, on general grounds, taking experimental energy bins smaller than the energy resolution is questionable. For this reason in order to perform either the shape or the mirror test described above we will require that the widths of the two energy intervals involved are larger than the energy resolution.

In the case of DAMA, due to the large statistics we will assume that the two independent

determinations of $\tilde{\eta}_1$, indicated with $\tilde{\eta}_{1,1}$ and $\tilde{\eta}_{1,2}$, have Gaussian fluctuations. Denoting with σ_1 and σ_2 the corresponding statistical errors, we will then require, as in [22]:

$$\Delta_{ST} \equiv \frac{|\tilde{\eta}_{1,1} - \tilde{\eta}_{1,2}|}{\sqrt{\sigma_1^2 + \sigma_2^2}} \leq 1.64, \quad (4.4)$$

at the 95 % C.L.

The other experiments claiming some excess that we will discuss in the following (CRESST and CDMS-*Si*) are not sensitive to the annual modulation but only to absolute (time-averaged) rates; moreover their statistics is much reduced compared to DAMA. In this case we assume Poissonian fluctuations when comparing the two mirror energy bins. Let us indicate them with `E_SIG` and `M_E_SIG`. In order to check if two independent count rates N_1 and N_2 belong to two Poisson distributions with averages λ_1 and λ_2 the conditional test by Przyborowski and Wilenski can be adopted[29]. In particular the p-value for the hypothesis $\lambda_1/\lambda_2 \leq c$ is given by:

$$p = \sum_{i=N_1}^{N_1+N_2} \binom{N_1+N_2}{i} [f(c)]^i [1-f(c)]^{N_1+N_2-i}, \quad (4.5)$$

with $f(c) = c/(1+c)$. At 95% C.L. we will then require $p \geq 0.05$ with:

$$\frac{\lambda_1}{\lambda_2} \leq c = \frac{\int_0^\infty dE_{ee} \mathcal{R}_{\text{E_SIG}}(E_{ee})}{\int_0^\infty dE_{ee} \mathcal{R}_{\text{M_E_SIG}}(E_{ee})}. \quad (4.6)$$

We conclude this Section by noting that a different type of internal check is needed in the case of multi-target experiments, such as DAMA and CRESST. As pointed out in Section 2 in this case the factorization of the halo model dependence is only possible if dominance of scatterings off one single target can be established. Consider for instance *NaI* in DAMA: the energy range of the signal is mapped into two different v_{min} ranges corresponding to scatterings off *Na* and *I*, i.e.: `E_SIG` \rightarrow `V_SIG_NA`, `V_SIG_I`. When m_{DM} is small enough one has dominance of scatterings off *Na* since `V_SIG_NA` \subset `V_GAL` and `V_SIG_I` $\not\subset$ `V_GAL`. On the other hand at higher values of the WIMP mass the situation occurs when `V_SIG_NA`, `V_SIG_I` \subset `V_GAL` with `V_SIG_I` $>$ `V_SIG_NA`. In the standard situation where a Maxwellian velocity distribution and a scalar coupling with $f_n/f_p=1$ are assumed one has $\tilde{\eta}_1(\text{V_SIG_I}) \ll \tilde{\eta}_1(\text{V_SIG_NA})$ but the (small) ratio $\tilde{\eta}_1(\text{V_SIG_I})/\tilde{\eta}_1(\text{V_SIG_NA})$ is fixed in the Maxwellian case, so that the scaling law in (2.4) overcomes it in favour of dominance of scatterings off Iodine. Notice, however, that if no assumptions are made on the functional form of $\tilde{\eta}_1$ it is in principle possible to assume that whenever `V_SIG_I` \cap `V_SIG_NA` $= \emptyset$ either $\tilde{\eta}_1(\text{V_SIG_I})$ or $\tilde{\eta}_1(\text{V_SIG_NA})$ is small enough to allow for dominance of the other target. Notice that $\tilde{\eta}_1$ is not required to be decreasing with v_{min} and can have in principle any functional form.

The situation of multi-target experiments observing an excess in $\tilde{\eta}_0$ is slightly more constrained, due to the requirement that $\tilde{\eta}_0$ is decreasing with v_{min} . Given two targets `E_SIG` \rightarrow `V_SIG_TARGET_1`, `V_SIG_TARGET_2` and whenever the scaling law favours `TARGET_2`, dominance of `TARGET_1` is realized if $\tilde{\eta}_0(\text{V_SIG_TARGET_2}) \simeq 0$. However this requires `V_SIG_TARGET_2` $>$ `V_SIG_TARGET_1` strictly. Of course a particular case of this is the stronger requirement `V_SIG_TARGET_2` $>$ v_{esc} (notice that for inelastic scattering this does not automatically mean that `TARGET_2` is the heavier target, since, when $\delta \neq 0$, v_{min} in Eq. (2.1) is no longer necessarily increasing with the target mass).

4.2 Comparison among different experiments

As discussed in Section 3 for the elastic case, present DM data show tension between excesses on $\tilde{\eta}_0$ and $\tilde{\eta}_1$ and constraints on $\tilde{\eta}_0$, and the extent of the discrepancy is particularly strong if an Isothermal Sphere model for the WIMP velocity distribution is assumed. In particular, inspection of Figs. 1 and 2 shows that, when no model is assumed for the velocity distribution, an experiment can constrain another one if it is sensitive to the same v_{min} interval, or to *lower* values (the latter condition descending from the requirement that $\tilde{\eta}_0$ is decreasing monotonically with v_{min}). However, both the condition that $v_{min} < v_{esc}$ in the range explaining a possible excess, and the degree of overlapping between two experiments using different target materials depend on the mapping between E_R and v_{min} , which, according to Eq.(2.1), in the IDM scenario can be modified by assuming $\delta \neq 0$. In particular, if for the same choice of m_{DM} and δ conflicting experimental results can be mapped into non-overlapping ranges of v_{min} and if the v_{min} range of the constraint is at higher values compared to the excess (while that of the signal remains below v_{esc}) the tension between the two results can be eliminated by an appropriate choice of the $\tilde{\eta}_{0,1}$ functions in compliance with the conditions of Eq. (4.3). This, of course, at the price of having to assume that $\tilde{\eta}_0$ and $\tilde{\eta}_1$ drop to appropriately low values in the (high) v_{min} range pertaining to the constraint.

The requirements expressed above can be expressed in a compact form by making use of the notation introduced at the beginning of this Section. Suppose that one experiment measures an excess over the background in the energy interval E_SIG while the result of the search of a second experiment is null in the energy range E_BOUND . Then to have compatibility between the signal interpretation and the experimental bound, given $E_SIG \rightarrow V_SIG$, $E_BOUND \rightarrow V_BOUND$, one needs to impose the two conditions: $V_SIG \subset V_GAL$ and $V_BOUND > V_SIG$.

5 Phenomenological analysis: the case of inelastic scattering

In this Section we wish to extend the results of Section 3 to the inelastic case, by making use of the criteria introduced in Section 4. In order to proceed, we first notice that, as explained in Section 2, the effect of mapping energies to velocities using Eq.(2.1) with $\delta \neq 0$ is only to shift the $\tilde{\eta}_{1,2}$ determinations in the v_{min} space compared to the $\delta=0$ case, without changing their normalization (with the exception of moderate changes due to possible modifications in the data binning). As a consequence of this, we can conclude that, at least qualitatively, we expect the hierarchy in the impacts of different constraints as observed in Figs.1 and 2 to be preserved in the case of inelastic scattering, with XENON100, LUX and the SuperCDMS remaining the most constraining bounds, in particular between one and three orders of magnitude below the DAMA result. So our approach will be to first explore systematically the $m_{DM}-\delta$ parameter space to find regions where the XENON100, LUX and the SuperCDMS constraints are relaxed, and then to pick within those regions some representative benchmark points where to discuss in more detail the experimental situation including all the other bounds.

On the other hand, notice that, as already pointed out in our Introduction, while the discrepancy between KIMS and the DAMA interpretation in terms of WIMP- I scatterings appears to be quantitatively less severe, in this case it cannot be relieved by assuming the IDM scenario. Something similar happens between the CoGeNT effect and other bounds obtained with Germanium detectors. For this reason we will include the CoGeNT effect and the KIMS bound in all the relevant plots, but we will not consider them in our discussion of compatibility ranges in the $m_{DM}-\delta$ parameter space.

In the following we will analyze the IDM parameter space using the parameter ranges:

$$1 \text{ GeV} \leq m_{DM} \leq 1 \text{ TeV}, -300 \text{ keV} \leq \delta \leq 300 \text{ keV}. \quad (5.1)$$

5.1 Sodium scattering in DAMA and the CDMS-Si excess

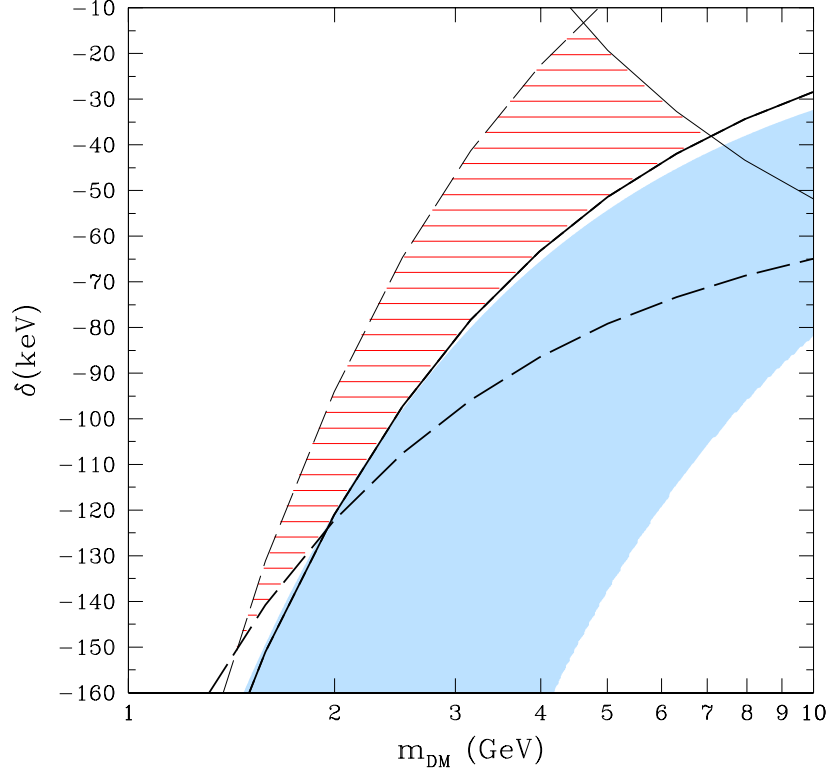


Figure 4. Mass splitting $\delta = m'_{DM} - m_{DM}$ as a function of m_{DM} . The horizontally (red) hatched area represents the IDM parameter space where the modulation effect measured by DAMA assuming scattering on Sodium corresponds to a $v_{min} < v_{esc}$ range which is always below the corresponding one probed by LUX and XENON100. As explained in the text, in this case Xenon experiments can constrain the DAMA excess only when some assumptions are made on the galactic velocity distribution. The enclosed region is the result of the combination four boundaries (see Section 4.2): the thin solid line where $v_{min}(E_{min}^{LUX}) = v_{min}^{Na}(E_{max}^{DAMA})$; the thick solid line where $v_{min}(E_{min}^{LUX}) = v_{min}^{Na}(E_{min}^{DAMA})$; the thin long-dashed line where $v_{min}^{Na}(E_{max}^{DAMA}) = v_{esc}$; the thick long-dashed line where $v_{min}^{Na}(E_{min}^{DAMA}) = v_{esc}$. The blue shaded strip represents points for which $\Delta_{ST} > 1.64$, where Δ_{ST} is the shape-test parameter defined in Eq.(4.4). The corresponding boundaries for XENON100 are less constraining and lie outside the boundaries of the figure. In all the shown m_{DM} - δ interval the v_{min} range corresponding to an explanation of the DAMA effect with WIMP scatterings off Iodine targets extends beyond the escape velocity.

Let us indicate with $\mathbf{V_DAMA_Na} \equiv [v_{min}^{DAMA,Na}, v_{max}^{DAMA,Na}]$ the v_{min} range for the DAMA signal assuming scattering on Sodium, and with $\mathbf{V_DAMA_I} \equiv [v_{min}^{DAMA,I}, v_{max}^{DAMA,I}]$ the corresponding one for scattering on Iodine. $\mathbf{V_LUX} \equiv [v_{min}^{LUX}, v_{max}^{LUX}]$ represents the range to which LUX is sensitive, while $\mathbf{V_XENON100} \equiv [v_{min}^{XENON100}, v_{max}^{XENON100}]$ is the same for XENON100 (see appendix A for experimental details).

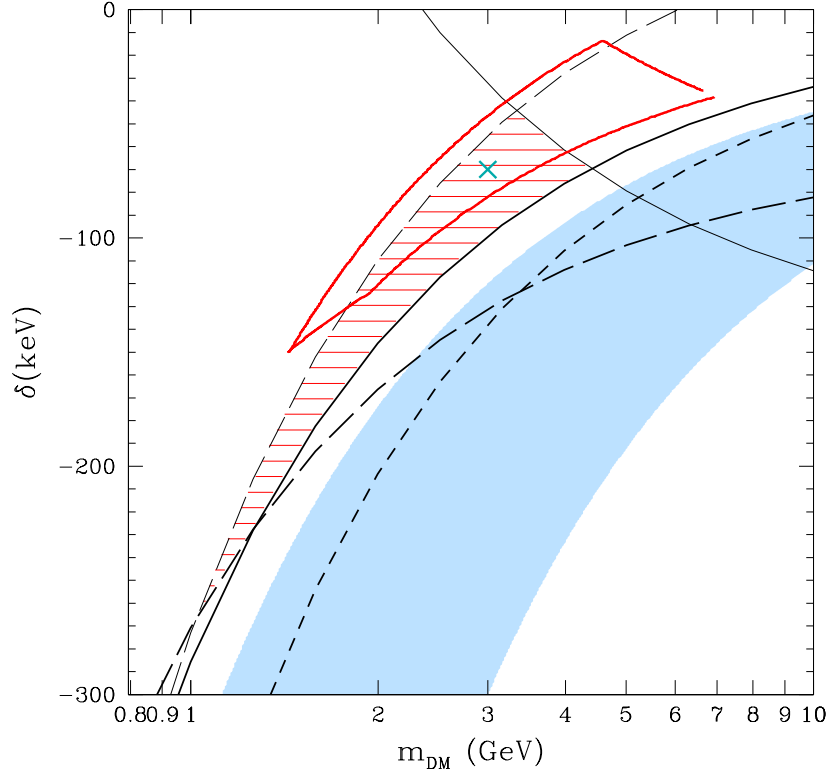


Figure 5. Same as in Fig. 4 for the Silicon target in CDMS [8]. The horizontally (red) hatched area represents the IDM parameter space where the excess measured by CDMS-*Si* corresponds to a $v_{min} < v_{esc}$ range which is always below the corresponding one probed by LUX and XENON100. As explained in the text, in this case Xenon experiments can constrain the CDMS-*Si* excess only when some assumptions are made on the galactic velocity distribution. The enclosed region is the result of the combination of four conditions: the thin solid line where $v_{min}(E_{min}^{LUX}) = v_{min}(E_{max}^{CDMS-Si})$; the thick solid line where $v_{min}(E_{min}^{LUX}) = v_{min}(E_{min}^{CDMS-Si})$; the thin long-dashed line where $v_{min}(E_{max}^{CDMS-Si}) = v_{esc}$; the thick long-dashed line where $v_{min}(E_{min}^{CDMS-Si}) = v_{esc}$. The corresponding boundaries for XENON100 are less constraining: in particular the thin short-dashed line represents the parameter space where $v_{min}(E_{min}^{XENON100}) = v_{min}(E_{min}^{CDMS-Si})$. The blue shaded strip represents points excluded by the mirror test introduced in Section 4.1 where $p < 0.05$, with p defined in Eq.(4.5). The closed solid (red) contour is the same compatibility region shown in Fig. 4. The cross represents the benchmark point whose $v_{min}-\tilde{\eta}_{0,1}$ parameter space is discussed in Figs 6.

The result of our analysis is shown in Fig. 4, where we use $Q_{Na}=0.3$ for the Sodium quenching factor (see Appendix A). In the whole $m_{DM}-\delta$ range we find $V_{DAMA_I} \cap V_{GAL} = \emptyset$, so that the assumption of dominance of scatterings off Sodium is consistent. Moreover in the region between the two long-dashed lines $V_{DAMA_NA} \subset V_{GAL}$, i.e. the required values of v_{min} to explain the signal with scatterings on Sodium are all below v_{esc} : in particular, the thick long-dashed line corresponds to $v_{min}(E_{min}^{Na}) = v_{esc}$, while the thin long-dashed line to $v_{min}(E_{max}^{Na}) = v_{esc}$. In the same figure the (light-blue) shaded area is excluded by the shape test described in Section 4.1 (the shaded area extends beyond the region with $V_{DAMA_NA} \subset V_{GAL}$ because in that domain only a fraction of the signal interval is automatically selected to do the test, while the remaining part, or a fraction of it, corresponds to v_{min} values larger

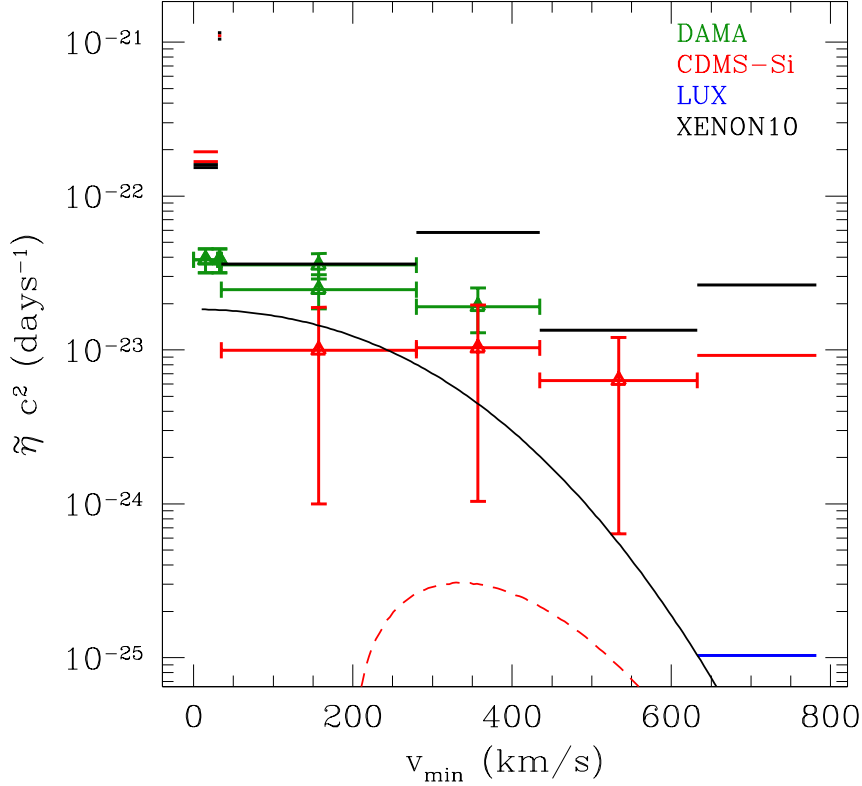


Figure 6. Measurements and bounds for the functions $\tilde{\eta}_0$ and $\tilde{\eta}_1$ for the benchmark point $m_{DM} = 3$ GeV, $\delta = -70$ keV, represented with a cross in Fig. 5, and assuming isospin violation $f_n/f_p = -0.79$. The solid (black) and dashed (red) lines represent the predictions for $\tilde{\eta}_0$ and $\tilde{\eta}_1$, respectively, for a Maxwellian velocity distribution, normalized to the most constraining upper bound.

than v_{esc}). Moreover, in the region above the thick solid line (corresponding to $v_{min}(E_{min}^{Na}) = v_{min}(E_{min}^{LUX})$) and below the thin solid line (corresponding to $v_{min}(E_{max}^{Na}) = v_{min}(E_{min}^{LUX})$) one has $V_{LUX} > V_{DAMA_NA}$. Notice that in both cases the boundaries are determined by the light response of LUX at threshold, and that this issue for liquid dual-phase scintillators is still controversial [24]. On the other hand the same boundaries from XENON100 are less constraining (due to the higher lower threshold) and lie outside the plot. The overlapping of the two regions $V_{DAMA_NA} \subset V_{GAL}$ and $V_{LUX} > V_{DAMA_NA}$ is not affected by the shape test and in Fig. 4 is given by the horizontally (red) hatched area. In this region LUX can constrain the DAMA excess only if our knowledge on the $\tilde{\eta}_0$ function allows us to extrapolate it from the LUX range down to the DAMA-*Na* range. If on the other hand no assumptions are made about $\tilde{\eta}_0$ besides (4.3) the two results can be made compatible for a wide range of $\tilde{\eta}_0$ functional forms. Notice that this argument involves exclusively kinematics, and is valid no matter what the dynamics of the process is. This means in particular that it would hold also if the scaling law of the WIMP-nucleus cross section were different from the one given in Eq.(2.4), and/or the dynamics were modified by some other effect, such as, for instance, the exchange of a light mediator or a magnetic-type coupling, introducing a dependence of the differential rate on the recoil energy and/or the incoming WIMP velocity different from

the one given in Eq.(2.2) ⁸.

The same check can be made between DAMA scatterings on Sodium and the SuperCDMS experiment bound[16] which uses a Germanium target. Proceeding as before, indicating by $\mathbf{V_SUPERCDMS} \equiv [v_{min}^{SuperCDMS}, v_{max}^{SuperCDMS}]$ the corresponding v_{min} interval, we have checked that $\mathbf{V_SUPERCDMS} \leq \mathbf{V_DAMA}$ over all the $m_{DM}-\delta$ range of Eq. (5.1), i.e. SuperCDMS is always sensitive to v_{min} values in the same range or smaller than those which could explain the DAMA effect. This means that, besides experimental issues, the two measurements cannot be reconciled using kinematics arguments only. However, in presence of some additional dynamical mechanism suppressing WIMP scatterings on Germanium compared to that on Sodium, DAMA and SuperCDMS can in principle be reconciled. An example of such mechanism is the Isospin violation mechanism[31], where a specific choice of the f_n/f_p ratio in Equation (2.4) can suppress the WIMP coupling to targets within a restricted range of Atomic numbers: in particular, by choosing $f_n/f_p \simeq -0.79$ ⁹ the SuperCDMS bound (as well as those of all other experiments using Ge targets) would no longer be present.

In Fig.5 we repeat the same analysis by comparing the excess of three events claimed by the CDMS-*Si* experiment[8] to LUX, XENON100 and SuperCDMS. The result turns out to be qualitatively similar to the previous case. By indicating with $\mathbf{V_CDMS_SI} \equiv [v_{min}^{CDMS-Si}, v_{max}^{CDMS-Si}]$ the v_{min} interval that can explain the CDMS-*Si* excess, in Fig. 5 the region between the two long-dashed lines has $\mathbf{V_CDMS_SI} \subset \mathbf{V_GAL}$ (the thick long-dashed line corresponds to $v_{min}(E_{min}^{CDMS-Si}) = v_{esc}$ while the thin long-dashed line to $v_{min}(E_{max}^{CDMS-Si}) = v_{esc}$). On the other hand in the region above the thick solid line (corresponding to $v_{min}(E_{min}^{CDMS-Si}) = v_{min}(E_{min}^{LUX})$) and below the thin solid line (corresponding to $v_{min}(E_{max}^{CDMS-Si}) = v_{min}(E_{min}^{LUX})$) one has $\mathbf{V_LUX} > \mathbf{V_CDMS_SI}$. Similarly to what happens in Fig.4 the same boundaries for XENON100 are less constraining due the higher energy threshold: however in this case the curve corresponding to $v_{min}(E_{min}^{CDMS-Si}) = v_{min}(E_{min}^{XENON100})$ lies within the plot and is represented by the thick short-dashed line. The overlapping of the two regions $\mathbf{V_CDMS_SI} \subset \mathbf{V_GAL}$ and $\mathbf{V_LUX} > \mathbf{V_CDMS_SI}$ is given by the horizontally (red) hatched area and is not affected by the (light-blue) shaded area excluded by the mirror test introduced in Section 4.1 (notice that in the case of the three events in CDMS-*Si* the shape-test is obviously not as constraining as in the DAMA case).

Similarly to what happened in Fig.4 also in the case of Fig.5 one has $\mathbf{V_SUPERCDMS} \leq \mathbf{V_CDMS_SI}$ over all the shown $m_{DM}-\delta$ range. Again, a possibility to reconcile CDMS-*Si* and SuperCDMS is to assume the same suppression mechanism for WIMP scattering on Ge advocated in the discussion of Fig.4. Actually, in Fig. 5 the closed solid (red) contour represents the same compatibility region shown in Fig.4 for DAMA-*Na*. Since the two regions overlap, one may wonder whether compatibility among the two excesses (DAMA-*Na* and CDMS-*Si*) can actually be achieved in compliance with constraints from other null results. For this reason in Fig.6 we plot the measurements and bounds on the functions $\tilde{\eta}_0$ and $\tilde{\eta}_1$ for the benchmark choice $m_{DM} = 3$ GeV, $\delta = -70$ GeV (corresponding to the cross plotted in Fig.5) and for $f_n/f_p \simeq -0.79$ to comply with the SuperCDMS bound. As shown in the Figure, indeed, the DAMA-*Na* and CDMS-*Si* can be separately brought into agreement with other experimental constraints for the same choice of m_{DM} and δ . In the same figure the solid (black) line represents the $\tilde{\eta}_0$ function in the case of a Maxwellian velocity distribution

⁸As discussed in [30] in the case of a generalized interaction a factorizable definition of the η function different from Eq.(2.7) would still be possible.

⁹Next-to-leading order corrections in the chiral expansion of the effective WIMP-quark interaction can modify the value of the f_n/f_p ratio for which the cancellation takes place[32].

normalized to the LUX upper bound, and the dashed (red) curve the corresponding prediction for $\tilde{\eta}_1$. From this plot it is clear that for an Isothermal Sphere model even by assuming isospin violation it is not possible to separately reconcile DAMA and CDMS-*Si* with both LUX and SuperCDMS, but this can in principle be achieved if no assumptions are made on the velocity distribution. However, even in this case DAMA and CDMS-*Si* appear in tension with each other, since the $\tilde{\eta}_1$ ranges explaining DAMA-*Na* are systematically larger than the $\tilde{\eta}_0$ ranges required to explain the CDMS-*Si* excess (in disagreement to the last of conditions (4.3)).

Notice that in some of the v_{min} intervals of Fig. 6 DAMA provides two independent determinations of $\tilde{\eta}_1$, a consequence of the double mapping of Eq.(2.1), and that these determinations appear to be in mutual agreement (as confirmed by the fact that for this specific choice of m_{DM} and δ we find the shape test parameter value $\Delta_{ST} \simeq 0.95$).

5.2 Iodine scattering in DAMA and the CRESST excess

In this section we will assume Iodine scattering in DAMA and Tungsten scattering in CRESST. As already pointed out previously and shown in Fig. 2, a tension arises in this case between DAMA and KIMS and since both experiments use the same Iodine target nuclei this discrepancy cannot be solved by changing the particle-physics model of the WIMP interaction. On the other hand, as we will see, the tension with at least some of the other experiments can in this case be alleviated by a combination of particle physics assumptions and by allowing a generalized WIMP velocity distribution complying with the minimal set of assumptions summarized in Eq. (2.11).

The result of a scanning of the m_{DM} - δ parameter space assuming Iodine scattering in DAMA is shown in Fig. 7. In all the shown range $V_{DAMA_NA} \cap V_{GAL} = 0$ while in the horizontally hatched domain $V_{DAMA_I} \subset V_{GAL}$. Moreover, the (light-blue) shaded areas are excluded by the shape test. In this case DAMA regions compatible to both LUX and SuperCDMS, can be found. In particular, in the $+45^\circ$ hatched region $V_{LUX} > V_{DAMA_I}$, while in the -45° hatched area $V_{SUPERCDMS} < V_{DAMA_I}$, i.e., in this case the marked region corresponds to the excluded one. However, in the same figure no regions of compatibility between DAMA and XENON100 can be found. This result is in agreement to the analysis of Ref.[22]. One comment is in order here. The boundary of the $+45^\circ$ hatched region in Fig. 7 is determined by a combination of the two conditions: $v_{min}(E_{max}^{LUX}) = v_{min}(E_{min}^{DAMA})$ and $v_{min}(E_{max}^{LUX}) = v_{min}(E_{max}^{DAMA})$, i.e. the boundary of that region is determined by the upper edge of the LUX analyzed energy interval ($S1=30$ PE, see Appendix A). In this Section we adopt the value $Q_I=0.07$ for the Iodine quenching factor (see Appendix A). This value, which is within the large systematic uncertainties on Q_I , reduces the tension between DAMA and LUX by increasing $E_{min}^{DAMA}=2$ keV/ Q_I , reducing $v_{min}(E_{min}^{DAMA})$ and making the condition $v_{min}(E_{max}^{LUX}) > v_{min}(E_{min}^{DAMA})$ easier to achieve. Notice also that the upper end of the analyzed spectrum in liquid Xenon detectors is chosen to avoid the background from cosmogenic ^{127}Xe [34], so is common also to XENON100. However, mainly due to the larger light yield in LUX ($L_y=8.8$ PE) compared to that in XENON100 ($L_y=2.28$ PE) when converted in KeVnr the upper bound of the XENON100 Region of Interest is significantly larger than that for LUX (adopting the experimental inputs summarized in Appendix A one gets $E_R^{max}=43.04$ keVnr for XENON100 vs. $E_R^{max}=24.9$ keVnr for LUX). For this reason in this case XENON100 is more constraining than LUX. Notice that since the higher part of the analyzed spectrum in XENON100 is not fraught by the many systematic uncertainties which characterize the region close to threshold[24] one should expect the ensuing constraints to be robust. However, in the spirit of minimizing the tension between DAMA and other

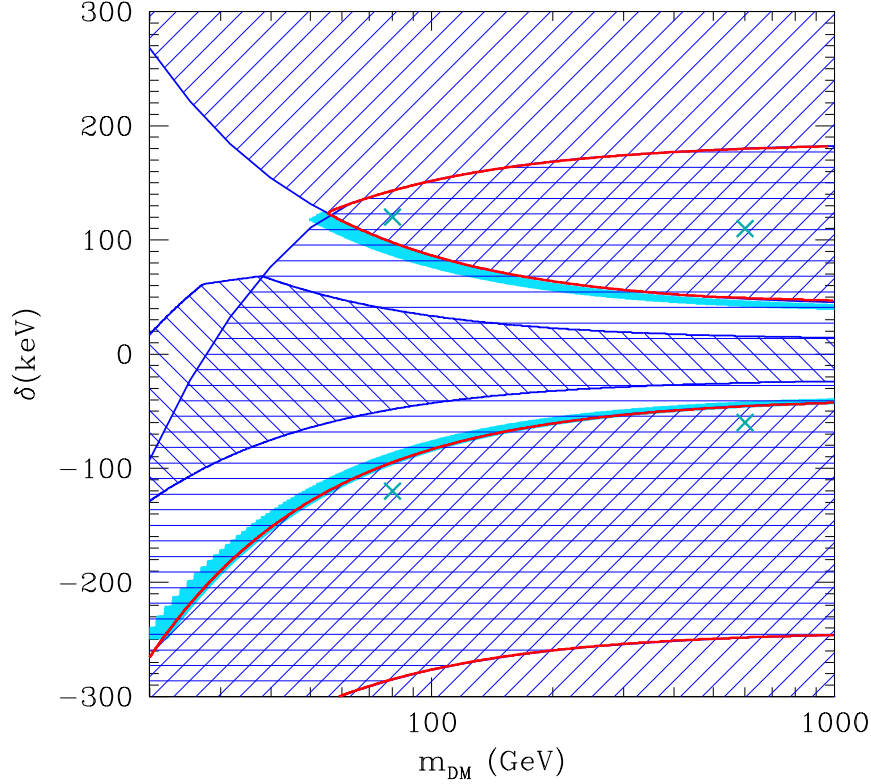


Figure 7. Same as in Fig. 4 for the I target in DAMA [2]. The region enclosed by the thick solid (red) line represents the IDM parameter space where the excess measured by DAMA corresponds to a $v_{min} < v_{esc}$ range which is always below the corresponding ones probed by LUX[10] and SuperCDMS[16]. The enclosed region is the result of the combination of three conditions: in the region with horizontal hatches the whole v_{min} range corresponding to the DAMA signal is below v_{esc} ; $+45^\circ$ oblique hatches correspond to the domain where the v_{min} range probed by LUX is at higher values compared to the range explaining DAMA; in the region with -45° oblique hatches the v_{min} range probed by SuperCDMS overlaps or is at lower values compared to the range explaining DAMA. The blue shaded strip represents points where $\Delta_{ST} > 1.64$, where Δ_{ST} is the shape-test parameter defined in Eq. (4.4). In all the shown m_{DM} - δ interval the v_{min} range corresponding to an explanation of the DAMA effect with WIMP scatterings off Sodium targets extends beyond the escape velocity. The four crosses are the benchmark points whose v_{min} - $\tilde{\eta}_{0,1}$ parameter space is discussed in Figs. 8(a-d).

experiments by reducing it to that with the minimal number of other experiments (in this case KIMS and XENON100), in Fig.7 we single out the regions where DAMA is compatible with LUX and SuperCDMS with a thick (red) boundary. Within those boundaries we select four benchmark points marked by crosses in Figure 7 and we adopt them to analyze the experimental data, getting estimations of the $\tilde{\eta}_0$ and $\tilde{\eta}_1$ functions in Figure 8(a-d) (assuming $f_n/f_p=1$). In all the plots of Fig. 8 we also show the ranges of the $\tilde{\eta}_0$ function which can explain the CRESST effect, where scatterings on Tungsten are assumed to be dominant. Notice that while, as expected in all the plots of Fig. 8(a-d) the DAMA points are compatible with the other constraints (except KIMS and XENON100), in these particular benchmarks points CRESST is incompatible with LUX and XENON100.

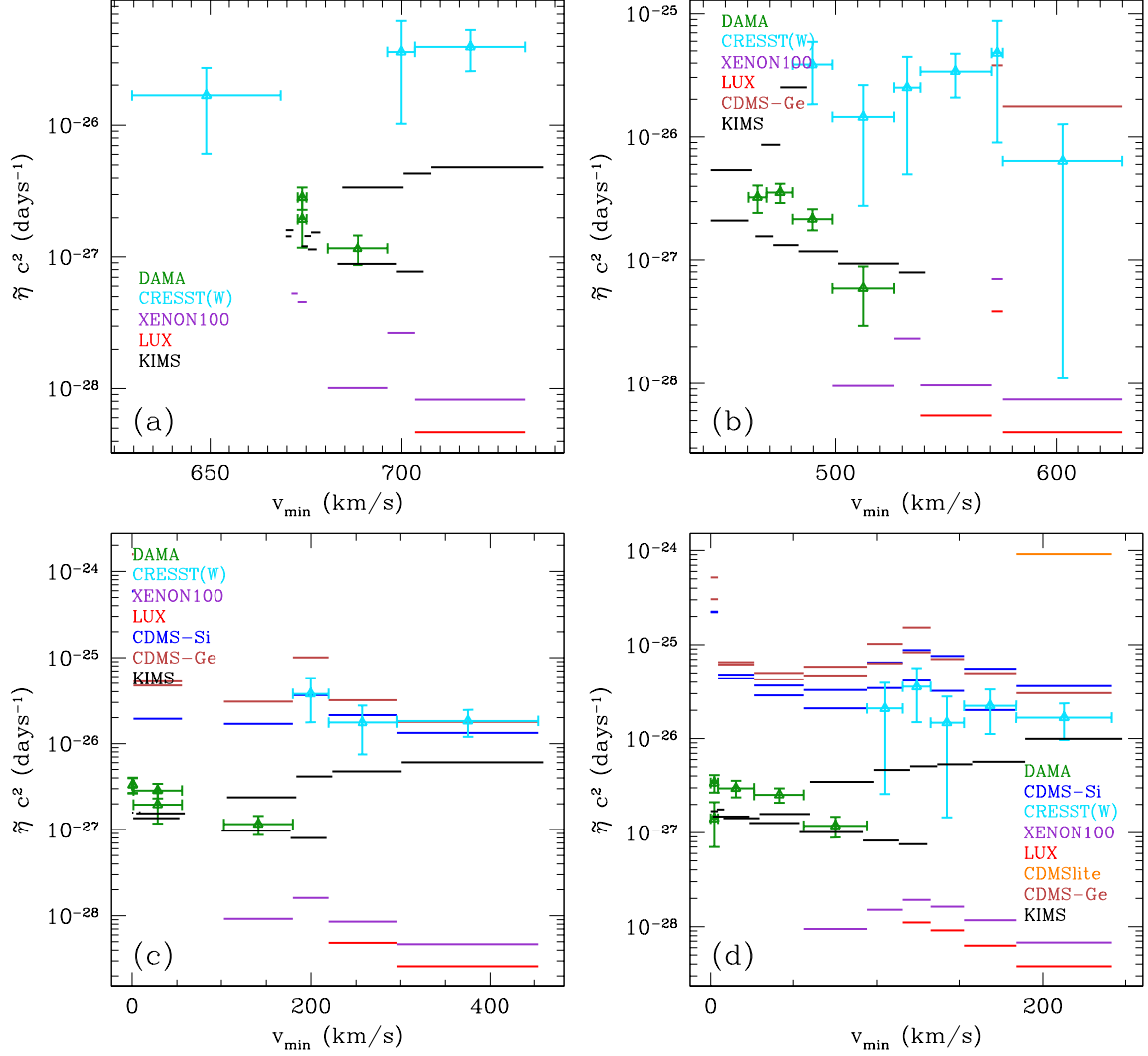


Figure 8. Measurements and bounds for the functions $\tilde{\eta}_0$ and $\tilde{\eta}_1$ for the four benchmark points represented with crosses in Fig.7 and for $f_n/f_p=1$. (a) $m_{DM}=80$ GeV, $\delta=120$ keV; (b) $m_{DM}=600$ GeV, $\delta=110$ keV; (c) $m_{DM}=80$ GeV, $\delta=-120$ keV; (d) $m_{DM}=600$ GeV, $\delta=-60$ keV. In all these benchmarks the tension between DAMA and other experiments is maximally alleviated, since it is reduced to that with the minimal number of other experiments (KIMS and XENON100).

The corresponding analysis of the IDM parameter space where the CRESST excess is assumed to be explained with WIMP scatterings off Tungsten targets is shown in Fig.9. Let us indicate with $V_{\text{CRESST-W}}=[v_{\min}^{\text{CRESST,W}}, v_{\max}^{\text{CRESST,W}}]$ the v_{\min} range where WIMP- W scatterings correspond to the signal region in CRESST. In Fig.9 the region with horizontal hatches contains configurations for which $V_{\text{CRESST-W}} \subset V_{\text{GAL}}$. Tungsten is by large the heaviest among the targets in CaWO_4 , so if, for instance, $f_n/f_p=1$, the scaling law given by Eq.(2.4) implies that in this region we can safely assume that W scatterings dominate over other targets (see Fig.12(a)). Notice that the four benchmark points selected in Fig.7 are all contained in this domain, so that in all the plots of Fig.8 the assumption of W domination is consistent. Moreover, in the $+45^\circ$ hatched region of Fig.9 $V_{\text{XENON100}} > V_{\text{CRESST-W}}$

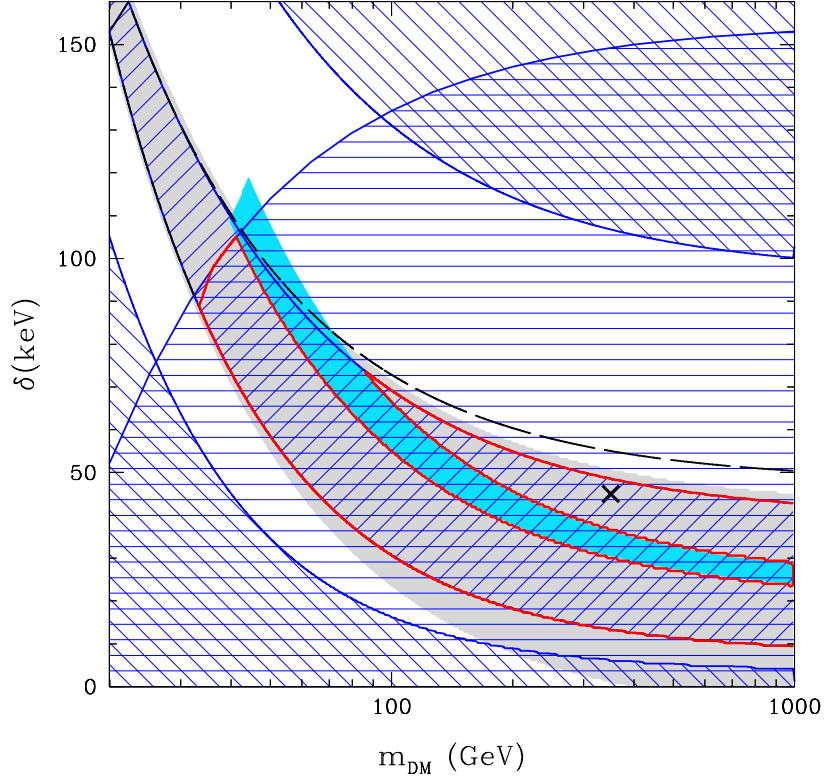


Figure 9. Same as in Fig. 4 for the Tungsten target in CRESST [9]. The region enclosed by the thick solid (red) line represents the IDM parameter space where the excess measured by CRESST corresponds to a $v_{min} < v_{esc}$ range which is always below the corresponding ones probed by XENON100[11], LUX[10], SuperCDMS[16] and KIMS[13], and is not excluded by the mirror test introduced in Section 4.1. The enclosed region is the result of the combination of four conditions: in the region with horizontal hatches the whole v_{min} range corresponding to the CRESST signal is below v_{esc} ; +45° oblique hatches correspond to the domain where the v_{min} range probed by XENON100 is at higher values compared to the range explaining CRESST (the bound from LUX is slightly less constraining and the upper part of the corresponding closed region is represented by the dashed (black) line); in the region with -45° oblique hatches the v_{min} range probed by SuperCDMS overlaps or is at lower values compared to the range explaining CRESST; the light (gray) shaded area corresponds to the domain where the v_{min} range probed by KIMS is at higher values compared to the range explaining CRESST. The blue shaded strip represents points where $p < 0.05$, with p defined in Eq.(4.5). In this figure v_{min} ranges corresponding to WIMP scatterings off Ca or O targets are not always beyond v_{esc} (see discussion of Fig. 11) so dominance of WIMP- W scatterings must be established dynamically. This is achieved, for instance, in the isospin-conserving case $f_n/f_p=1$, when the WIMP coupling to W nuclei is much larger than that on Ca and O (see Fig. 12(a)). The cross represents the benchmark point whose $v_{min}-\tilde{\eta}_{0,1}$ parameter space is discussed in Fig. 10.

(the bound from LUX is slightly less constraining and the upper part of the corresponding closed region where $V_{LUX} > V_{CRESST_W}$ is represented by the dashed (black) line), while in the -45° hatched area $V_{SUPERCDMS} < V_{CRESST_W}$, i.e., also in this case the marked region corresponds to the excluded one, and XENON100 turns out to be more constraining than SuperCDMS. Moreover, indicating with $V_{KIMS}=[v_{min}^{KIMS}, v_{max}^{KIMS}]$ the overall v_{min} to which the KIMS experiment is sensitive, in the same Figure the light (gray) shaded area represents

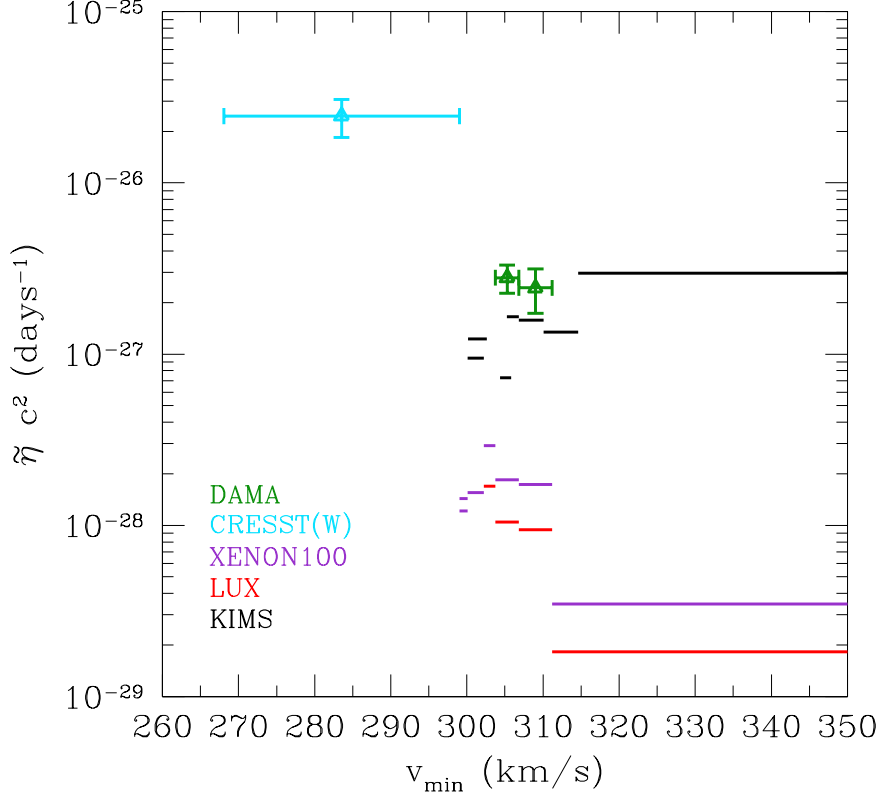


Figure 10. Measurements and bounds for the functions $\tilde{\eta}_0$ and $\tilde{\eta}_1$ for the benchmark point $m_{DM} = 350$ GeV, $\delta=45$ keV, represented with a cross in Fig.9(a), and assuming an isospin conserving coupling, $f_n/f_p=1$.

the parameter space where $V_{KIMS} > V_{CRESST_W}$, i.e. in that region the CRESST excess is not constrained by KIMS. Finally, the (light-blue) shaded area is excluded by the mirror test, which now carves away a part of the allowed region. In Fig.9 the two remaining domains compatible to all the requirements and constraints are marked by a thick (red) boundary. We then select within that domain a benchmark point (indicated by a cross) whose corresponding analysis in the $v_{min}-\tilde{\eta}_{0,1}$ space is shown in Fig.10: indeed inspection of that figure shows that in this case CRESST complies with all other constraints.

In order to see if DAMA-*I* and CRESST-*W* can be explained by the same IDM parameters and be compatible to the other experimental constraints, in Fig.11 we superimpose the two regions allowed by DAMA-*I* and CRESST-*W* when the LUX and XENON100 bounds are not applied. Again, in this case one needs to assume some mechanism to suppress the WIMP coupling to *Xe* targets, such as $f_n/f_p \simeq -0.69$. However, as shown in the right panel of Fig.12, the particular choice $f_n/f_p \simeq -0.69$ not only suppresses the WIMP coupling to Xenon targets, but it also enhances the same coupling to Calcium nuclei, so that in principle now the condition $V_{CRESST_W} \subset V_{GAL}$ no longer ensures dominance of scatterings off *W* nuclei in *CaWO*₄. However, indicating with V_{CRESST_CA} the v_{min} interval for scatterings off Ca nuclei, the region above the short-dashed line of Fig.11 corresponds to $V_{CRESST_CA} \cap V_{GAL} = \emptyset$ (the region where the same happens for scatterings off Oxygen targets is above the long-dashed curve) so that in that domain *W* dominance can be consistently assumed. The DAMA-CRESST

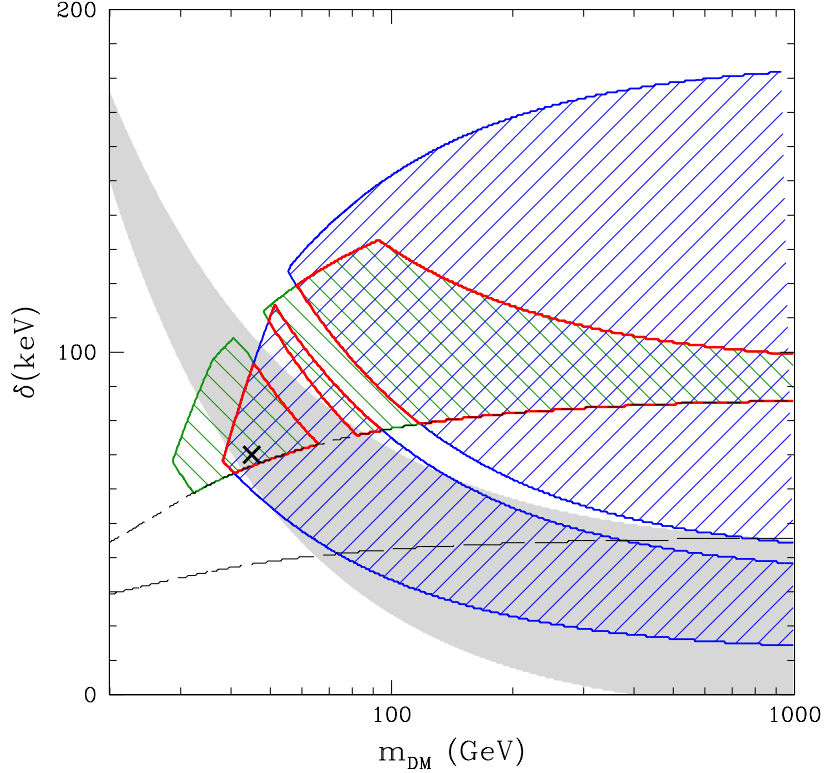


Figure 11. Superposition of allowed regions for WIMP scattering off Iodine in DAMA (+45° blue-hatched area) and off Tungsten in CRESST (-45° green-hatched area), when the Xenon bounds (LUX and XENON100) are not included. If some mechanism is advocated to suppress WIMP couplings on Xenon targets the region enclosed by the thick (red) line represents the parameter space where both the DAMA and CRESST effects correspond to $v_{min} < v_{esc}$ ranges which are always below the corresponding one probed by SuperCDMS[16]. Specifically, if isospin violation, $f_n/f_p \simeq -0.69$, is assumed to suppress WIMP couplings on Xe targets, the coupling of WIMPs to Ca is enhanced compared to that on W (see Fig. 12)(b) so in order to assume dominance of WIMP- W scatterings the region above the curve with short-dashes must be considered, where the v_{min} range corresponding to WIMP- Ca scatterings is beyond v_{esc} (the region above the line with long-dashes corresponds to the same condition for WIMP- O scatterings). Finally the light (gray) shaded area corresponds to the domain where the v_{min} range probed by KIMS is at higher values compared to the range explaining CRESST. The cross represents the benchmark point whose $v_{min}-\tilde{\eta}_{0,1}$ parameter space is discussed in Fig. 13.

regions complying to all these bounds and requirements are marked in Fig. 11 by the thick (red) boundaries. In particular one of the two regions overlaps with the light (gray) shaded band where also the requirement $V_{KIMS} > V_{CRESST_W}$ is satisfied. The cross in the latter domain represents a benchmark that we analyze in the $v_{min}-\tilde{\eta}_{0,1}$ space in Fig. 13: inspection of that figure shows that in this case compatibility between DAMA and CRESST is achieved in compliance with SuperCDMS. Moreover, although the tension between DAMA and KIMS persists as expected, now the CRESST excess and the KIMS bound are mutually compatible.

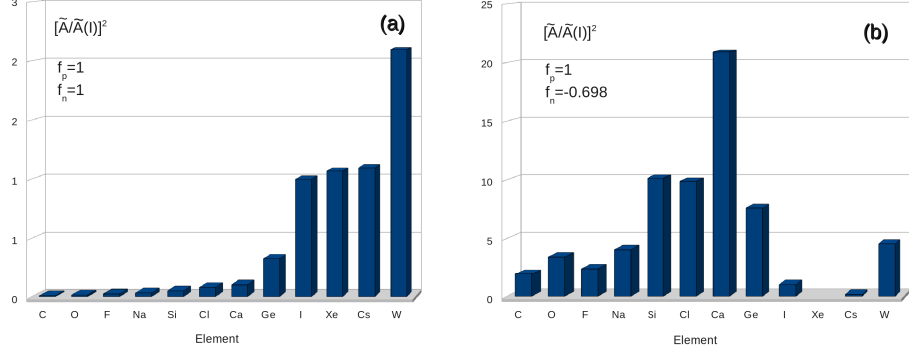


Figure 12. Scaling law defined in Eq.(2.4) (normalized to that for WIMP- I scattering) for the nuclear targets considered in the present analysis. **(a)** Isospin conserving case ($f_n/f_p=1$). **(b)** Isospin violating case $f_n/f_p=-0.698$, corresponding to the maximal suppression of the WIMP coupling to Xe targets.

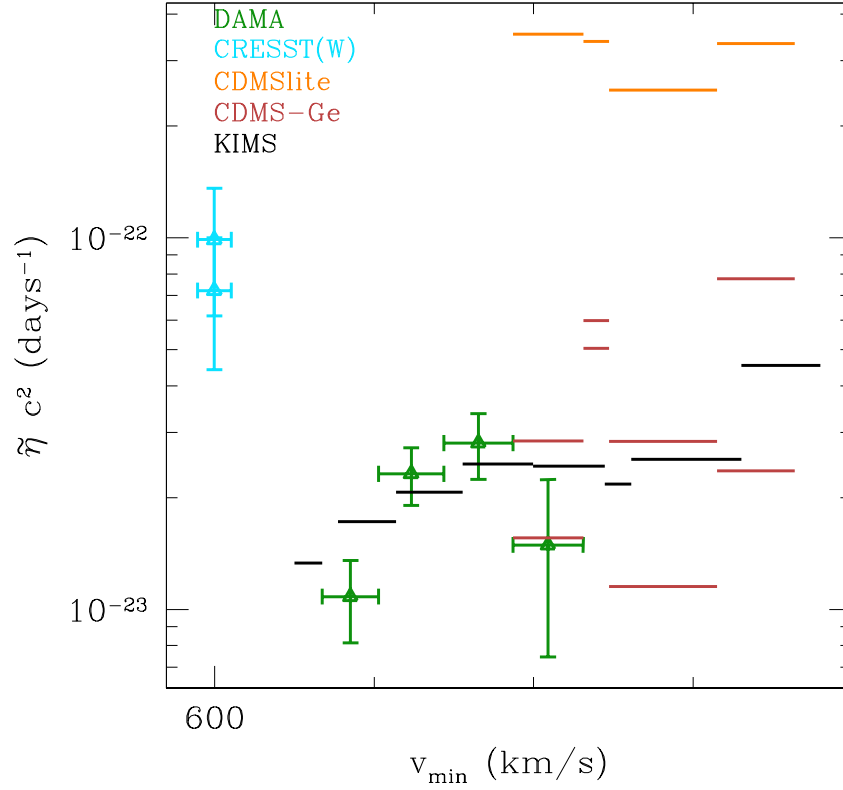


Figure 13. Measurements and bounds for the functions $\tilde{\eta}_0$ and $\tilde{\eta}_1$ for the benchmark point $m_{DM} = 45$ GeV, $\delta=70$ keV, represented with a cross in Fig.11, and assuming an isospin violating coupling, $f_n/f_p=-0.69$

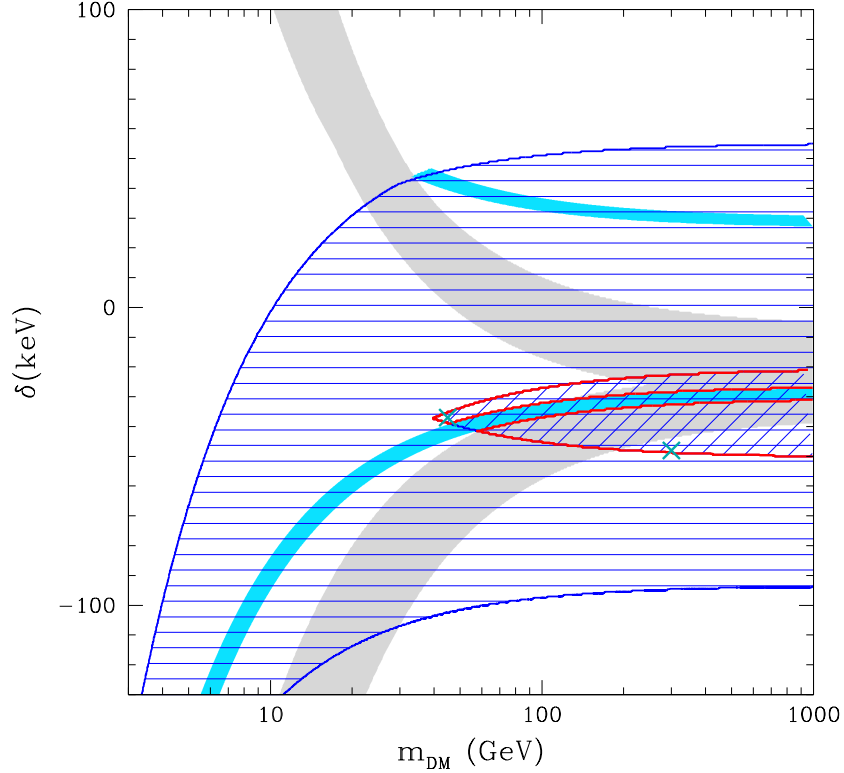


Figure 14. Same as in Fig. 4 for the Sodium target in DAMA [8], but assuming the Na quenching factor from Ref.[38] (see Appendix A). The two regions enclosed by the thick solid (red) line represent the IDM parameter space given by the combination of two requirements: (i) that the excess measured by DAMA corresponds to a v_{min} range which is always below the corresponding one probed by SuperCDMS (the corresponding domain is represented by $+45^\circ$ hatches); (ii) the region is not excluded by the shape test introduced in Section 4.1 (the shaded (light-blue) bands correspond to $\Delta_{ST} > 1.64$). The area represented by horizontal hatches shows the parameter space where the $v_{min} < v_{esc}$ range explaining DAMA is all below v_{esc} . In this figure XENON detectors bounds are not included. The light (gray) shaded region represents the parameter space where the v_{min} ranges mapped by scatterings off Na and I do not overlap: in this case dominance of scatterings off any of the two targets in NaI is possible (see discussion in Section 5.3). The two crosses are the benchmark points whose $v_{min}-\tilde{\eta}_{0,1}$ parameter space is discussed in Figs. 15(a-b).

5.3 Sodium scattering in DAMA at large WIMP masses

As discussed at the end of Section 4.1, for a Maxwellian velocity distribution and when $f_n/f_p=1$, WIMPs heavier than approximately 20 GeV interact in DAMA predominantly by scattering off Iodine targets. However, if $f_p/f_n \neq 1$ and when a wider class of galactic velocity distributions is allowed, WIMP- Na scatterings can dominate also for heavier WIMP masses. In this case DAMA and KIMS can decouple also at large values of m_{DM} . Mainly motivated by this possibility, in this Section we wish to explore this scenario in more detail.

In Section 5.1 we already pointed out that within all the $m_{DM}-\delta$ range of Eq. (5.1) we found $V_{SUPERCDMS} \leq V_{DAMA}$, so that the SuperCDMS constraint could not be decoupled from the DAMA effect if scattering off Na nuclei was assumed. Nevertheless, that result was obtained by assuming $Q_{Na}=0.3$ for the Sodium quenching factor, and it has to be pointed

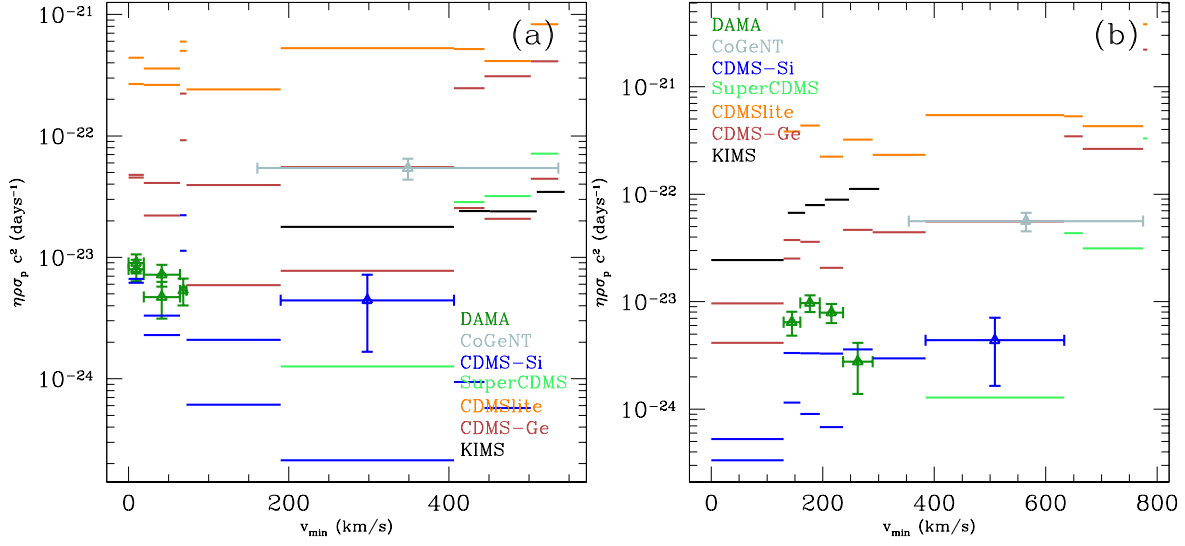


Figure 15. Measurements and bounds for the functions $\tilde{\eta}_0$ and $\tilde{\eta}_1$ for the two benchmark points represented with crosses in Figs.7(a-b) and for $f_n/f_p = -0.69$. (a) $m_{DM} = 45$ GeV, $\delta = -37$ keV; (b) $m_{DM} = 300$ GeV, $\delta = -48$ keV.

out that the measurement of the latter is presently somewhat controversial. In particular in Ref. [38] a determination of Q_{Na} significantly smaller than previous ones is discussed. In this Section we will repeat the analysis of Section 5.1 using this latter determination (see Appendix A for details). The result is shown in Fig. 14 where in the horizontally hatched region $V_{DAMA_NA} \subset V_{GAL}$, while, as a consequence of the different quenching factor, in the $+45^\circ$ hatched domain now $V_{SUPERCDMS} > V_{DAMA_NA}$ is possible. However now we find that $V_{LUX} \leq V_{DAMA_NA}$ over all the (5.1) ranges for the parameters. Nevertheless, one can again assume $f_n/f_p \simeq -0.69$ to suppress the WIMP coupling to Xenon. In this case this region of the parameter space can be in agreement with both constraints. Notice that, as shown in Fig. 12, this particular choice of f_n/f_p has also the effect of suppressing the couplings of WIMPs to Iodine and Cesium compared to that to Sodium, so that in this range dominance of scatterings off Na can be consistently assumed in NaI and also the KIMS constraint can be relieved. Moreover, in Fig. 14 the light (gray) shaded region represents the parameter space where $V_{DAMA_NA} \cap V_{DAMA_I} \neq \emptyset$. As discussed in Section 4.1, no matter which WIMP- Xe coupling suppression mechanism is assumed, outside that band dominance of Na (actually, of any of the two targets) in DAMA can be assumed, albeit at the price of tuning the $\tilde{\eta}_1(v_{min})$ to a sufficiently small value in the v_{min} ranges mapped by I . Notice that the same range of v_{min} would also interest scatterings of WIMPS off CsI in part of the energy range analyzed by KIMS, so that this would be another way to (at least) reduce the tension between KIMS and DAMA. Finally, in Fig. 14 the (light-blue) shaded area is excluded by the shape test.

The thick (red) boundary encloses the areas subject to all the requirements and constraints. Within those boundaries we select two benchmark points, marked by crosses, that are analyzed in the $v_{min} = \tilde{\eta}_{0,1}$ parameter space in Figs. 15(a-b). Notice that in Fig. 11 it was possible to find a region in the $m_{DM} - \delta$ parameter space where WIMPs dominantly scatter off Tungsten nuclei in CRESST, in spite of the enhanced coupling to Calcium for the choice $f_n/f_p \simeq -0.69$. This was possible because in that Figure $\delta > 0$: in that case for Calcium and

Oxygen v_{min}^* is larger than for Tungsten, and driven beyond v_{esc} for δ large enough, leaving only the contribution of W nuclei. In the case of Fig. 14, however, the region allowed by the SuperCDMS bound corresponds to $\delta < 0$. In this case $v_{min}^*=0$ and there is no longer a clear-cut hierarchy among the v_{min} ranges pertaining to the three different targets. The same thing happens for the scaling-law factors, which in CaWO_4 scale as $\tilde{A}_{Ca} : 4 \times \tilde{A}_O : \tilde{A}_W = 1 : 0.54 : 0.22$. This means that a complicated pattern of dominances depending not only on m_{DM} and δ , but also on the recoil energy is expected in this case, intertwined with domains of the parameter space where the factorization introduced in Section 2 is not possible in the first place. For this reason in Figs. 15(a-b) CRESST is not included in the discussion. Inspection of Figs. 15(a-b) reveals that, as expected, the discrepancy between DAMA and KIMS is relieved. Moreover, as required, the SuperCDMS bound is no longer effective on the DAMA points. Nevertheless a tension develops in this case between DAMA and the CDMS-*Si* data (Fig. 15(a)) or both the CDMS-*Si* and the CDMS-*Ge* data (Fig. 15(b)).

6 Conclusions

In the Inelastic Dark Matter scenario, the halo-model factorization approach used to compare results from Dark Matter direct detection experiments is more complicated than in the elastic case, because in presence of a mass splitting $\delta \neq 0$ the mapping between the nuclear recoil energy E_R and the minimal velocity v_{min} that the incoming WIMP needs to have to deposit E_R becomes more involved than in the elastic case. For this reason a systematic analysis of IDM where all available data are included making use of the factorization property of the halo-model dependence was still missing so far. In the present paper we have attempted to address this issue, introducing some strategies to determine regions in the IDM parameter space where the tension existing among different experimental results can be (at least partially) alleviated.

To this aim we have first introduced some internal consistency checks involving the data of one single experiment, which exploit the fact that, when the same v_{min} range is mapped in two different energy intervals, the expected correlation can be compared with the data. Moreover, we have argued that, if a minimal set of assumptions is adopted for the WIMP velocity distribution, the tension between the putative signal from an experimental excess and the constraint from a null result can be reduced or eliminated provided that the two results can be mapped into non-overlapping ranges of v_{min} and if the v_{min} range of the constraint is at higher values compared to that of the excess. We stress that this latter argument involves exclusively kinematics, and is valid no matter what the dynamics of the process is.

We have then shown that, in the elastic case, the constraints from XENON100, LUX and SuperCDMS are the most binding, and argued that this hierarchy among limits is preserved in the IDM case. Then, adopting the two criteria summarized above, we have systematically explored the IDM parameter space to find regions where the XENON100, LUX and the SuperCDMS constraints are relaxed, and picked within those regions some representative benchmark points where we have discussed in more detail the experimental situation including all the other bounds.

Following the strategy outlined above, we have then singled out five scenarios:

- i) $2 \text{ GeV} \lesssim m_{DM} \lesssim 4 \text{ GeV}$, $-130 \text{ keV} \lesssim \delta \lesssim -45 \text{ keV}$ (see Fig. 5): in this approximate domain both an explanation of the DAMA modulation effect through WIMP-*Na* scattering and the excess of three WIMP-candidate events observed by CDMS-*Si* can be

brought in agreement with other bounds if some dynamical mechanism such as isospin violation can be advocated to suppress WIMP interaction with Germanium. However, the DAMA and CDMS-*Si* results turn out to be in mutual tension.

- ii) $m_{DM} \gtrsim 60$ GeV, $50 \text{ keV} \lesssim \delta \lesssim 180 \text{ keV}$; a wide band with $\delta \lesssim -40 \text{ keV}$ (see Fig.7): in this approximate domain the tension between an explanation of the DAMA modulation effect in terms of WIMP–Iodine scattering can be alleviated by reducing it to that with the minimal number of other experiments: KIMS (which uses the same target nucleus) and XENON100 (which turns out to be more constraining than LUX thanks to the higher value of the upper bound of its analyzed energy region in keVnr). Notice that in the usual case when an Isothermal Sphere model for the velocity distribution is assumed, besides KIMS and XENON100 the DAMA region at large m_{DM} appears to be well inside the domain excluded also by LUX and/or SuperCDMS (depending on the δ parameter). This may be interpreted as to strengthen the robustness of the exclusion, in spite of the many uncertainties existing in each experiment when taken separately. In our analysis we have shown that sometimes this argument can be misleading, and the number of experiments necessarily in tension with DAMA at large WIMP masses can be lower than generally assumed.
- iii) $m_{DM} \gtrsim 30$ GeV, $10 \text{ keV} \lesssim \delta \lesssim 100 \text{ keV}$ (see Fig.9) : in this approximate domain the excess measured by CRESST[9] can be made compatible with all other constraints.
- iv) $m_{DM} \gtrsim 350$ GeV, $50 \text{ keV} \lesssim \delta \lesssim 130 \text{ keV}$ (see Fig.11). Mutual compatibility can be achieved between DAMA and CRESST in compliance with other constraints with the exception of KIMS. The size of the corresponding region in the m_{DM} – δ parameter space varies depending on the f_n/f_p parameter.
- v) If a measurement of the Sodium quenching factor substantially smaller compared to other measurements is adopted[38] and assuming a suppression mechanism for the WIMP–Xenon coupling, it is possible to single out a region of the parameter space with $m_{DM} \gtrsim 40$ GeV, $-50 \text{ keV} \lesssim \delta \lesssim -20 \text{ keV}$ where WIMP–Sodium scattering dominates in DAMA (see Fig. 14). In this regime the SuperCDMS bound is evaded and also KIMS is not constraining. However, now DAMA appears in tension with CDMS-*Si* and CDMS-*Ge*.

All the compatibility regions listed above cannot be achieved if a standard Isothermal Sphere is adopted for the WIMP velocity distribution.

We conclude by pointing out that direct detection experiments are affected by many sources of possible systematic errors (including the many uncertainties connected to quenching factors, atomic form factors, background cuts efficiencies, etc.) that may affect significantly the compatibility regions listed above. For instance, in the specific example of Section 5.3 we have shown that the adoption of a different measurement of the Sodium quenching factor can lead to a very different scenario for the allowed parameter space.

Acknowledgments

This work was supported by the National Research Foundation of Korea(NRF) grant funded by the Korea government(MOE) (No. 2011-0024836).

A Experimental inputs for the analysis

In this Appendix we summarize the experimental inputs that we have used to evaluate the response function defined in Eq.(2.14) for each of the experiments included in our analysis. Whenever applicable we will follow the convention to indicate with E_R the true recoil energy, with E_{ee} the electron-equivalent energy ($E_{ee} = Q(E_R)E_R$ with Q the quenching factor) and with E' the visible energy, as introduced in Section 2. In the case of bolometric measurements (CDMS, CRESST) we assume $Q = 1$. With the exceptions of LUX and XENON100 we model the energy resolution with a Gaussian and we indicate the corresponding variance.

DAMA We have taken the modulation amplitudes in 0.5 keVee bins from Fig.6 of Ref.[2] (already normalized to counts/day/kg/keV for a total exposure of 1.17 ton yr), adopting the signal region $2 \text{ keVee} \leq E' \leq 4 \text{ keVee}$ in all plots and when discussing the ranges of v_{min} in Section 5. Moreover, in order to perform the mirror test introduced in Section 4.1 we have used the extended range $2 \text{ keVee} \leq E' \leq 20 \text{ keVee}$. We have adopted the value $Q_I=0.07$ for the quenching factor for Iodine¹⁰, while we have assumed two different determinations for the quenching factor for Sodium: in Section 5.1 we have used $Q_{Na}=0.3$, while in Section 5.3 we have adopted the determination shown in Fig. 9 of Ref.[38] fitting the experimental points with the functional form $Q_{Na}(E_R) = 0.024 * \sqrt{E_R/\text{keVnr}}$. For the energy resolution we have taken $\sigma_{DAMA} = 0.0091(E'/\text{keVee}) + 0.448\sqrt{E'/\text{keVee}}$ in keVee.

XENON100 and LUX In the case of LUX we have assumed zero WIMP candidate events in the range $2 \text{ PE} \leq S_1 \leq 30 \text{ PE}$ in the lower half of the signal band, as shown in Fig. 4 of Ref. [10] for the primary scintillation signal S_1 (directly in Photo Electrons, PE) for an exposure of 85.3 days and a fiducial volume of 118 kg of Xenon. On the other hand for XENON100 we assumed the spectrum from Fig. 2 of [11], consisting in two events at $S_1=[3.3 \text{ PE}, 3.8 \text{ PE}]$ in the experimental range $3 \text{ PE} \leq S_1 \leq 30 \text{ PE}$ for an exposure of 224.6 days and a fiducial volume of 34 kg. In both cases, following Ref. [39] (see Eqs. (14-15)) we have modeled the detector's response with a Poissonian fluctuation of the S_1 scintillation photoelectrons combined with a Gaussian resolution $\sigma_{PMT}=0.5 \text{ PE}$ for the photomultiplier so that the response function defined in Eq.(2.14) is modified into:

$$\mathcal{R}_{[S_{1,min}, S_{1,max}]} = \frac{N_T m_N \tilde{A}^2}{2\mu_{\chi N}^2} F^2(E_R) MT \times \quad (\text{A.1})$$

$$\int_{S_{1,min}}^{S_{1,max}} dS_1 \sum_{n=1}^{\infty} \text{Gauss}(S_1|n, \sqrt{n}\sigma_{PMT}) \text{Poiss}[n, \nu(E_R)] \xi_{cuts}(S_1). \quad (\text{A.2})$$

In the equation above $\text{Poiss}(n, \lambda) = \lambda^n/n! \exp(-\lambda)$, while ξ_{cuts} represents the combination of a 50% acceptance combined with the quality cut efficiency (taken from Fig. 9 of [10] for LUX and from Fig.1 of [11] for XENON100). Moreover the expected number of PE for a given recoil energy E_R is given by:

$$\nu(E_R) = E_R \times L_{eff}(E_R) \times L_y \frac{S_{nr}}{S_{ee}}, \quad (\text{A.3})$$

with $L_y=8.8 \text{ PE}$ for LUX and $L_y=2.28 \text{ PE}$ for XENON100. For LUX we have taken $L_{eff}(E_R)$ from [40] (where it is calculated including the effect of the electric field, so that $S_{nr} = S_{ee} = 1$,

¹⁰We choose $Q_I=0.07$ to maximize the compatibility regions shown in Figs. 7 and 9. While presently the DAMA collaboration uses $Q_I=0.09$, the value $Q_I=0.07$ was adopted by DAMA in its early papers [35], while a value as low as $Q_I=0.05$ is quoted in [36]. Our choice is within the large systematic uncertainties on Q_I [37].

and assumed to vanish for $S_1 < 3$ PE), while for XENON100 we have taken $L_{eff}(E_R)$ from [41] (in this case $S_{nr}=0.95$ and $S_{ee}=0.58$).

CoGeNT We do not consider the annual modulation but only the spectral excess and take both the total count rates and the background from Fig. 23 of [6]¹¹ rescaling them to the latest exposure of 1129 days of Ref. [42] for a fiducial mass of 0.33 kg of Germanium and assuming the signal range $0.5 \text{ keVee} < E_{ee} < 2 \text{ keVee}$. For the quenching factor we assume $Q_{Ge} = 0.2(E/\text{keVee})^{0.12}$ as given in [6] while for the energy resolution we use $\sigma_{CoGeNT}(E') = \sqrt{69.7^2 + 0.976(E'/\text{eV})}$ in eV [43].

CDMS-Si We take the full energy range $7 \text{ keVnr} < E_R < 100 \text{ keVnr}$ analyzed in [8] with an exposure of 140.2 kg day with a Silicon target. The three WIMP candidate events are observed at energies $E_R=8.2 \text{ keVnr}$, 9.5 keVnr and 12.3 keVnr , so when discussing the ranges v_{min} in Section 5.1 or the consistency checks in Section 4.1 we define the signal region $8 \text{ keVnr} < E_R < 12.5 \text{ keVnr}$. Since the energy resolution in CDMS-Si has not been measured we take $\sigma_{CDMS-Si}(E') = \sqrt{0.293^2 + 0.056^2(E'/\text{keVnr})}$ in keVnr from [44].

SuperCDMS We include the low-energy analysis of SuperCDMS[16] with a Germanium target in the energy range $1.6 \text{ keVnr} < E_R < 10 \text{ keVnr}$ with a total exposition of 577 kg day and 11 observed WIMP candidates. The energy resolution is given by $\sigma_{CDMS-Si}(E') = \sqrt{0.293^2 + 0.056^2(E'/\text{keVnr})}$ in keVnr[44]

XENON10 The analysis of XENON10 makes use of the secondary ionization signal S_2 only, with an exposition of 12.5 day and a fiducial mass of 1.2 kg. We take the scale of the recoil energy E_R and the recorded event spectrum in the energy range $1.4 \text{ keVnr} < E_R < 10 \text{ keVnr}$ directly from Fig. 2 of Ref. [12]. The energy resolution is given by: $\sigma_{XENON10} = E_R/\sqrt{E_R Q_y(E_R)}$ where $Q_y(E_R)$ is the electron yield that we calculate with the same choice of parameters as in Fig. 1 of [12].

CDMSlite CDMSlite[15] analyzes the very low range $0.170 \text{ keVee} < E_{ee} < 7 \text{ keVee}$ for the electron-equivalent energy using a fiducial mass of 0.6 kg of Germanium and an exposition of 10.3 days. We take the spectrum from Fig. 1 of Ref. [15]. We adopt the same quenching factor that we use for CoGeNT, an energy resolution $\sigma_{CDMSlite} = 14 \text{ eV}$ and the efficiency $\xi_{cut} = 0.985$ [15].

CDMS-Ge We consider the data from detector T1Z5 in the range $2 \text{ keVnr} < E_R < 100 \text{ keVnr}$ available in digital format from [14] with a raw exposure of 35 kg day on Germanium target. The energy resolution is the same as in SuperCDMS, while the efficiency is taken from Fig.1 of Ref. [14].

CRESST We only focus on scatterings on Tungsten in CaWO_4 . To this aim we select from [9] the 45 events (out of 67) in the W recoil bands of Figs. 7, 9 and 17 in the total energy range $10 \text{ keVnr} < E_R < 40 \text{ keVnr}$ collected with an exposition of 730 kg day¹². The background in the W band is dominated by lead recoils from ^{210}Po decays, which we model as in Eq. (1) of Ref. [9]. When discussing v_{min} ranges in Section 5 and the consistency checks of Section 4.1 we select the signal region $12 \text{ keVnr} < E_R < 24 \text{ keVnr}$ where we optimize the signal/background ratio getting 34 total events vs. a background of 7.4. As far as the energy resolution is concerned, we use the two measurements $\text{FWHM}(E'=3.6 \text{ keVnr})$

¹¹We adopt the subtraction of background surface events from the official data analysis of the CoGeNT Collaboration[6]. For a critical independent assessment of the CoGeNT spectral excess, claiming a much less significant residual effect than the official analysis, see [7].

¹²After submission of the present manuscript new unpublished CRESST data have been presented in [33] that do not confirm the excess claimed in [9].

= 0.3 keV and $\text{FWHM}(E' = 64 \text{ keVnr}) = 1.6 \text{ keVnr}$ from [45] to fit the functional form $\sigma_{\text{CRESST}}(E') = -0.0442 + 0.0904\sqrt{E'}$ in keVnr ($\text{FWHD} = 2.355 \times \sigma$).

KIMS We take the 90% C.L. upper bounds on nuclear recoil events from Fig. 4 of Ref. [13] (for $3 \text{ keVee} < E' < 11 \text{ keVee}$ in 1-keVee bins, already in counts/day/kg/keV for an effective exposition of 24524.3 kg day) rebinning them using Eq.(4.2). We use as quenching factor the solid line in Fig.13 of Ref. [46] (in the measurement the quenching factors of Cs and I cannot be distinguished and are assumed to be the same). For the energy resolution we have rescaled the $\text{FWHM} \simeq 14.24 \text{ keVee}$ of the peak at 59.5 keVee from ^{241}Am calibration shown in Fig. 8 of Ref.[47], getting $\sigma_{\text{KIMS}}(E') = 0.78\sqrt{E'}$ in keVee. Since the atomic numbers of Iodine ($A=127$) and Cesium ($A=133$) are very close, both contributions can be incorporated in the definition of the response function, i.e.

$$\tilde{\eta} = \frac{\int_0^\infty dv_{\min} \tilde{\eta}(v_{\min}) \left[\mathcal{R}_{[E'_1, E'_2]}^{\text{Iodine}}(v_{\min}) + \mathcal{R}_{[E'_1, E'_2]}^{\text{Cesium}}(v_{\min}) \right]}{\int_0^\infty dv_{\min} \left[\mathcal{R}_{[E'_1, E'_2]}^{\text{Iodine}}(v_{\min}) + \mathcal{R}_{[E'_1, E'_2]}^{\text{Cesium}}(v_{\min}) \right]}. \quad (\text{A.4})$$

This of course can be done for any multi-target detector, but makes sense only when two response functions largely overlap, as in the case of CsI . The net effect is to somehow worsen in v_{\min} space the smearing effect of the energy resolution, but is practically irrelevant (we checked that it amounts to less than 3% on v_{\min} in all the benchmarks plotted). In particular, in the case $f_n/f_p = 1$ one has $\tilde{A}_{\text{Cesium}}/\tilde{A}_{\text{Iodine}} \simeq 1.1$, and the ensuing v_{\min} range is given by the combination of the (slightly offset) Cesium and Iodine mappings from the recoil energy to v_{\min} . However, in the case $f_n/f_p = -0.69$ discussed in Figs. 13 and 15 $\tilde{A}_{\text{Cesium}}/\tilde{A}_{\text{Iodine}} \simeq 0.15$ (see Fig. 12): in that particular case Iodine can be taken as the dominant target and the resulting v_{\min} ranges correspond to WIMP-Iodine scattering only.

References

- [1] P. A. R. Ade *et al.* [Planck Collaboration], arXiv:1303.5076 [astro-ph.CO].
- [2] R. Bernabei *et al.* [DAMA and LIBRA Collaborations], Eur. Phys. J. C **67**, 39 (2010) [arXiv:1002.1028 [astro-ph.GA]].
- [3] C. E. Aalseth *et al.* [CoGeNT Collaboration], arXiv:1401.3295 [astro-ph.CO].
- [4] Z. Ahmed *et al.* [CDMS Collaboration], arXiv:1203.1309 [astro-ph.CO].
- [5] Y. Kim, talk given at 13th International Conference on Topics in Astroparticle and Underground Physics, September 8–13 2013, Asilomar, California USA (TAUP2013).
- [6] C. E. Aalseth *et al.* [CoGeNT Collaboration], Phys. Rev. D **88**, no. 1, 012002 (2013) [arXiv:1208.5737 [astro-ph.CO]].
- [7] J. H. Davis, C. McCabe and C. Boehm, arXiv:1405.0495 [hep-ph].
- [8] R. Agnese *et al.* [CDMS Collaboration], Phys. Rev. Lett. **111**, 251301 (2013) [arXiv:1304.4279 [hep-ex]].
- [9] G. Angloher, M. Bauer, I. Bavykina, A. Bento, C. Bucci, C. Ciemniak, G. Deuter and F. von Feilitzsch *et al.*, Eur. Phys. J. C **72**, 1971 (2012) [arXiv:1109.0702 [astro-ph.CO]].
- [10] D. S. Akerib *et al.* [LUX Collaboration], arXiv:1310.8214 [astro-ph.CO].
- [11] E. Aprile *et al.* [XENON100 Collaboration], Phys. Rev. Lett. **109**, 181301 (2012) [arXiv:1207.5988 [astro-ph.CO]].

- [12] J. Angle *et al.* [XENON10 Collaboration], Phys. Rev. Lett. **107**, 051301 (2011) [Erratum-ibid. **110**, 249901 (2013)] [arXiv:1104.3088 [astro-ph.CO]].
- [13] S. C. Kim, H. Bhang, J. H. Choi, W. G. Kang, B. H. Kim, H. J. Kim, K. W. Kim and S. K. Kim *et al.*, Phys. Rev. Lett. **108**, 181301 (2012) [arXiv:1204.2646 [astro-ph.CO]].
- [14] Z. Ahmed *et al.* [CDMS-II Collaboration], Phys. Rev. Lett. **106**, 131302 (2011) [arXiv:1011.2482 [astro-ph.CO]].
- [15] , R. Agnese *et al.* [SuperCDMS Soudan Collaboration], Phys. Rev. Lett. **112**, 041302 (2014) [arXiv:1309.3259 [physics.ins-det]].
- [16] R. Agnese *et al.* [SuperCDMS Collaboration], arXiv:1402.7137 [hep-ex].
- [17] P. J. Fox, J. Liu and N. Weiner, Phys. Rev. D **83**, 103514 (2011) [arXiv:1011.1915 [hep-ph]].
- [18] C. McCabe, Phys. Rev. D **84**, 043525 (2011) [arXiv:1107.0741 [hep-ph]]; M. T. Frandsen, F. Kahlhoefer, C. McCabe, S. Sarkar and K. Schmidt-Hoberg, JCAP **1201**, 024 (2012) [arXiv:1111.0292 [hep-ph]].
- [19] P. Gondolo and G. B. Gelmini, JCAP **1212**, 015 (2012) [arXiv:1202.6359 [hep-ph]]; E. Del Nobile, G. B. Gelmini, P. Gondolo and J. -H. Huh, arXiv:1304.6183 [hep-ph]; E. Del Nobile, G. B. Gelmini, P. Gondolo and J. -H. Huh, JCAP **1403**, 014 (2014) [arXiv:1311.4247 [hep-ph]].
- [20] D. Tucker-Smith and N. Weiner, Phys. Rev. D **64**, 043502 (2001) [hep-ph/0101138].
- [21] P. W. Graham, R. Harnik, S. Rajendran and P. Saraswat, Phys. Rev. D **82**, 063512 (2010) [arXiv:1004.0937 [hep-ph]].
- [22] N. Bozorgnia, J. Herrero-Garcia, T. Schwetz and J. Zupan, JCAP **1307**, 049 (2013) [arXiv:1305.3575 [hep-ph]].
- [23] E. Aprile *et al.* [XENON100 Collaboration], Phys. Rev. D **84**, 061101 (2011) [arXiv:1104.3121 [astro-ph.CO]].
- [24] J. I. Collar, arXiv:1010.5187 [astro-ph.IM]; J. I. Collar, arXiv:1106.0653 [astro-ph.CO].
- [25] M. T. Frandsen, F. Kahlhoefer, C. McCabe, S. Sarkar and K. Schmidt-Hoberg, JCAP **1307**, 023 (2013) [arXiv:1304.6066 [hep-ph]]; M. McCullough and L. Randall, JCAP **1310**, 058 (2013) [arXiv:1307.4095 [hep-ph]]; M. T. Frandsen and I. M. Shoemaker, arXiv:1401.0624 [hep-ph]; G. B. Gelmini, A. Georgescu and J. -H. Huh, arXiv:1404.7484 [hep-ph].
- [26] R. H. Helm, Phys. Rev. **104**, 1466 (1956).
- [27] N. Fornengo and S. Scopel, Phys. Lett. B **576**, 189 (2003) [hep-ph/0301132].
- [28] E. Aprile *et al.* [XENON100 Collaboration], Phys. Rev. D **84**, 052003 (2011) [arXiv:1103.0303 [hep-ex]].
- [29] J. Przyborowski and H. Wilenski, Biometrika **31**, 313 (1940)
- [30] E. Del Nobile, G. Gelmini, P. Gondolo and J. -H. Huh, JCAP **1310**, 048 (2013) [arXiv:1306.5273 [hep-ph]].
- [31] A. Kurylov and M. Kamionkowski, Phys. Rev. D **69**, 063503 (2004) [hep-ph/0307185]; F. Giuliani, Phys. Rev. Lett. **95**, 101301 (2005) [hep-ph/0504157]; J. L. Feng, J. Kumar, D. Marfatia and D. Sanford, Phys. Lett. B **703**, 124 (2011) [arXiv:1102.4331 [hep-ph]].
- [32] V. Cirigliano, M. L. Graesser, G. Ovanessian and I. M. Shoemaker, arXiv:1311.5886 [hep-ph].
- [33] R. Strauss, talk given at the TeVPA/IDM Conference, Amsterdam, 23–28 June 2014, <http://indico.cern.ch/event/278032/session/12/contribution/109>.
- [34] M. Szydagis *et al.* [LUX Collaboration], arXiv:1402.3731 [hep-ex].
- [35] C. Bacci *et al.* [Beijing-Rome-Saclay (BRS) Collaboration], Phys. Lett. B **293**, 460 (1992).

- [36] K. Fushimi, H. Ejiri, H. Kinoshita, N. Kudomi, K. Kume, K. Nagata, H. Ohsumi and K. Okada *et al.*, Phys. Rev. C **47**, 425 (1993).
- [37] J. I. Collar, Phys. Rev. C **88**, no. 3, 035806 (2013) [arXiv:1302.0796 [physics.ins-det]].
- [38] J. I. Collar, Phys. Rev. C **88**, 035806 (2013) [arXiv:1302.0796 [physics.ins-det]].
- [39] E. Aprile *et al.* [XENON100 Collaboration], Phys. Rev. D **84**, 052003 (2011) [arXiv:1103.0303 [hep-ex]].
- [40] http://luxdarkmatter.org/talks/20131030_LUX_First_Results.pdf
- [41] E. Aprile *et al.* [XENON100 Collaboration], Phys. Rev. Lett. **107**, 131302 (2011) [arXiv:1104.2549 [astro-ph.CO]].
- [42] C. E. Aalseth *et al.* [CoGeNT Collaboration], arXiv:1401.3295 [astro-ph.CO].
- [43] C. E. Aalseth *et al.* [CoGeNT Collaboration], Phys. Rev. Lett. **101**, 251301 (2008) [Erratum-ibid. **102**, 109903 (2009)] [arXiv:0807.0879 [astro-ph]];
- [44] Z. Ahmed *et al.* [CDMS Collaboration], Phys. Rev. D **81**, 042002 (2010) [arXiv:0907.1438 [astro-ph.GA]].
- [45] http://wonder.lngs.infn.it/templates/wm_06_j15/download/Seidel_CRESSTwonder10.pdf
- [46] H. Park, D. H. Choi, J. M. Choi, I. S. Hahn, M. J. Hwang, W. G. Kang, H. J. Kim and J. H. Kim *et al.*, Nucl. Instrum. Meth. A **491**, 460 (2002) [nucl-ex/0202014].
- [47] H. S. Lee *et al.* [Kims Collaboration], Phys. Lett. B **633**, 201 (2006) [astro-ph/0509080].